



Master Thesis in Environmental Physics

Department of Physics and Electrical Engineering

University of Bremen

# REMOTE SENSING AND MODELLING OF $SO_2$ EMISSIONS FROM SAKURAJIMA VOLCANO

**Annika Katerina Tesio**

6421641

Supervisors

Dr. Andreas Richter

Prof. Dr. Mihalis Vrekoussis

- September 11, 2026 -

# Abstract

Volcanic $SO_2$ degassing poses a significant hazard to air quality and human health in populated areas near active volcanoes. Sakurajima, the most active volcano in Japan, affects a surrounding population of approximately 900,000 people. It is monitored by the Japan Meteorological Agency, but ground-based flux measurements are only performed sporadically, at most a few times per month. In a more general framework, ground-based monitoring networks such as the Network for Observation of Volcanic and Atmospheric Change (NOVAC) provide continuous measurements, but only at a limited number of well-instrumented volcanoes, and remain inherently restricted to the immediate vicinity of each source. This highlights the need for monitoring capabilities that can provide broader spatial coverage while retaining high temporal resolution.

Geostationary satellites offer a potential solution, providing hourly air quality products over wide regions. This thesis evaluates the use of the Geostationary Environment Monitoring Spectrometer (GEMS) L2 $SO_2$ product v3.0.1 for estimating $SO_2$ emission fluxes from Sakurajima, at hourly resolution, using the cross-section method. The study focuses on a two-week period (3–16 November 2023), coinciding with the VOLCOM ground-based measurement campaign.

A plume-identification and transect-based flux estimation procedure was developed and applied to GEMS retrievals, successfully identifying a plume in 49% of the analysed scans. The resulting hourly flux estimates, ranging between 0 and 100 t/h, showed consistent temporal trends across overlapping emissions from several scans, although some discrepancies between scans – including an apparent temporal shift – were also observed. Comparison with independent ground-based measurements from the VOLCOM campaign and the Japan Meteorological Agency revealed a systematic underestimation of GEMS-derived fluxes, on the order of 50t/h, not fully accounted for by the estimated uncertainty. Simulations with the FLEXPART-WRF dispersion model, initialised with the GEMS-derived emission estimates, reproduced a plume comparable in magnitude and general transport direction to the observed one, although spatially shifted by approximately 50 km, and failed to capture a near-source plume attributable to a known limitation of the plume-selection algorithm. Further analysis showed that the retrieved $SO_2$ VCD is highly sensitive to the assumed vertical distribution of $SO_2$,

suggesting that the operational GEMS retrieval, which does not explicitly account for volcanic sources, may not be well suited to elevated volcanic plumes.

These results indicate that GEMS is a promising tool for high-temporal-resolution monitoring of volcanic $SO_2$ emissions, while also highlighting specific limitations – related to plume selection, spatial resolution, and the assumed vertical a priori profile – that should be addressed in future refinements of the retrieval and estimation methods.

# Contents


**1 Introduction** **1**

**2 Theoretical background** **5**

2.1 Tropospheric $SO_2$ . . . . . 5

2.2 Differential optical absorption spectroscopy . . . . . 7

2.3 Methods for $SO_2$ flux estimation from satellite . . . . . 8

2.4 Atmospheric modelling . . . . . 10

**3 Methods** **13**

3.1 Study area . . . . . 13

3.2 Datasets & models . . . . . 14

3.2.1 Operational GEMS L2 $SO_2$ product v3.0.1 . . . . . 14

3.2.2 VOLCOM campaign . . . . . 15

3.2.3 JMA $SO_2$ flux . . . . . 16

3.2.4 ERA5 reanalysis . . . . . 16

3.2.5 WRF regional model . . . . . 17

3.2.6 FLEXPART-WRF model . . . . . 18

3.3 Analytical framework . . . . . 19

3.3.1 Overview of the work . . . . . 19

3.3.2 Cross-section method . . . . . 20

3.3.2.1 Uncertainty quantification . . . . . 22

**4 Results & discussion** **23**

4.1 Application of the cross-section method to GEMS retrieval . . . . . 23

4.1.1 Plume identification . . . . . 23

4.1.2 Transects definition . . . . . 26

4.1.3 $SO_2$ flux estimation . . . . . 30

4.2 Comparison with ground-based measurements . . . . . 33

4.3 Comparison to FLEXPART-WRF model simulation . . . . . 36

**5 Conclusions & outlook** **43**

**A Additional materials** **47**

**Bibliography** **47**

**Acknowledgments** **55**

# List of Figures


3.1 Sakurajima location and JMA $SO_2$ emissions . . . . . 14
3.2 Example driving routes of the VOLCOM campaign . . . . . 16
3.3 WRF domains . . . . . 18

4.1 GEMS product and plume selection method . . . . . 24
4.2 Noise criteria . . . . . 26
4.3 Example scans of unstable wind conditions exclusion criterion . . . . . 27
4.4 Transects definition . . . . . 28
4.5 Plume selection problem . . . . . 29
4.6 Plume selection problem . . . . . 30
4.7 $SO_2$ flux estimation of all scan on the 14th of November . . . . . 31
4.8 $SO_2$ flux estimation record for 14 November . . . . . 32
4.9 $SO_2$ flux estimates compared to ground-based measurements . . . . . 34
4.10 VCD computed from the FLEXPART-WRF model and from GEMS retrieval . . . . . 37
4.11 New GEMS VCD computed using the FLEXPART-WRF vertical profile 39
4.12 Recomputed and original GEMS AMF . . . . . 40
4.13 Detail of the AMF recalculation . . . . . 41

A.1 $SO_2$ flux estimation of individual scans . . . . . 48

LIST OF FIGURES

# Chapter 1

# Introduction

Volcanoes are an important component of the Earth system, acting as a conduit between the Earth's interior, its surface, and the atmosphere. Over geological timescales, volcanic activities have contributed to crustal development and to the evolution of the atmosphere. Volcanic emissions comprise a range of products, including lava, lahars, ash, and gases – primarily $H_2O$, $CO_2$, and $SO_2$.

While they play a fundamental role in Earth system processes, volcanoes remain a significant hazard to society. Approximately 70 volcanic eruptions occur worldwide each year [Wei, 2025], and exposure to volcanic hazards is widespread. In 1990, approximately 9% of the global population lived within 100 km of an active volcano [Small and Naumann, 2001]. Since 1700, volcanic activity has been associated with approximately 260,000 fatalities [Wei, 2025], resulting from processes such as lahars, pyroclastic flows, and ash fall, which can cause widespread destruction to human populations and infrastructure. Such destruction can, in turn, translate into substantial economic disruption. A notable example is the 2010 eruption of Eyjafjallajökull, in Iceland, when atmospheric transport carried the volcanic plume, including ash, across Europe. Because volcanic ash can damage aircraft engines, its dispersal led to the closure of European airspace, resulting in multi-billion-dollar economic losses [Budd et al., 2011; Gudmundsson et al., 2012].

Volcanic eruptions can also alter atmospheric composition and climate at larger scales. During sufficiently large, explosive eruptions, ash and $SO_2$ can be injected directly into the stratosphere, where they may reside long enough to influence Earth's radiative balance. The 1991 eruption of Mount Pinatubo in the Philippines provides a prominent example: the large amount of $SO_2$ injected into the stratosphere was gradually converted into sulfate aerosols, which have a long stratospheric lifetime and reflect incoming solar radiation, thereby producing a measurable global cooling effect [Robock, 2000]. Evidence for volcanic climate forcing is also available from paleoclimate studies, which identified periods of anomalous cooling associated with major historical eruptions., using records such as ice cores and tree rings [Sigl et al., 2015].

Beyond these episodic, large-scale impacts, significant volcanic gas emissions also occur outside of explosive eruptive phases. Volcanic degassing can be continuous or semi-continuous during periods of quiescence, as volatile gasses are released through vents. These persistent emissions are particularly relevant to air quality and human health, affecting populations living near active volcanoes and, under unfavourable atmospheric conditions, communities hundreds of kilometres downwind [Theys et al., 2013].

Among volcanic gases, $SO_2$ is of particular importance due to its impact on air quality and human health. Although $SO_2$ and the sulfate aerosols formed through its atmospheric oxidation have relatively short tropospheric lifetimes, they are among the most important volcanic air pollutants, contributing both through direct exposure to acidic gases and through the formation of fine particulate matter ($PM_{2.5}$). Exposure to volcanic air pollution has been associated with a range of acute and chronic health effects. This includes respiratory problems, aggravated asthma, reduced lung function, eye and skin irritation, and an increased hospitalisation rate for cardiovascular conditions. Sulfate aerosols also contribute to acid rain, which can acidify water supplies, damage crops and vegetation, and harm aquatic ecosystems, with severity depending on emission rates, meteorological conditions, and proximity to the source [Oppenheimer et al., 2011; Stewart et al., 2022; Carlsen et al., 2012].

Understanding the transport, and thus the spatial extent, of volcanic $SO_2$ plumes is therefore crucial for quantifying air quality hazards. $SO_2$ is a particularly effective tracer for volcanic plumes. Firstly, it is one of the major components of volcanic emissions. Second, unlike $H_2O$ and $CO_2$, which are already abundant and widely distributed in the atmosphere, $SO_2$ has a very low atmospheric background concentration. As a result, volcanic degassing typically produces $SO_2$ concentrations two orders of magnitude above background levels. Finally, $SO_2$ exhibits strong and distinctive absorption features in both the ultraviolet (UV) and thermal infrared (TIR) wavelength ranges [Theys et al., 2013]. Therefore it can be measured using either TIR or UV-visible spectroscopy; this study focuses on the latter .

In the 1960s, remote measurement of volcanic $SO_2$ emissions became possible using UV spectroscopy with the development of the correlation spectrometer (COSPEC), originally designed for monitoring industrial emissions of $SO_2$ and $NO_2$. Its application to volcanic monitoring showed that volcanic gas emissions could be quantified remotely rather than through in situ measurements [Stoiber and Jepsen, 1973]. This laid the foundation for the UV-visible remote sensing techniques used today, most notably the Differential Optical Absorption Spectroscopy (DOAS) technique [Platt and Stutz, 2008], which has since been implemented for a wide range of instrument geometries and platforms [Kern, 2025].

Different DOAS platforms offer distinct trade-offs between spatial and temporal

coverage. Ground-based instruments, deployed either at fixed locations or in mobile and airborne campaigns, can achieve high spatial and temporal resolution, but their coverage remains local and often depends on site accessibility. A notable example is the Network for Observation of Volcanic and Atmospheric Change (NOVAC), established in the early 2000s, which deploys a network of scanning DOAS instruments at volcanoes worldwide, to continuously and quantitatively monitor volcanic gas emissions. Although designed primarily for local hazard assessment, the openly available NOVAC data provided the first global dataset of volcanic emissions and enabled the validation of satellite-based $SO_2$ measurements [Galle et al., 2010]. Nonetheless, ground-based monitoring faces practical limitations, as many volcanoes are difficult to access, instrument deployment requires prior knowledge of the volcano's location, and both instruments and personnel can be exposed to volcanic hazards.

Satellite-based DOAS instruments address these limitations by offering much broader spatial coverage, independent of ground access, at the cost of lower spatial resolution. Polar-orbiting satellites, such as TROPOMI, OMI, and OMPS, provide global coverage on a daily basis, but their temporal resolution remains limited to one or two observations per day at a given location. A first step toward higher temporal resolution came with the Earth Polychromatic Imaging Camera (EPIC), launched in 2015 aboard the Deep Space Climate Observatory (DSCOVR). Positioned at the Sun-Earth Lagrange point L1, EPIC continuously observes the sunlit face of the Earth, capturing an image every 68–110 min [Marshak et al., 2018] – making it the first satellite to provide near-continuous, global-scale observations, albeit at a coarser spatial resolution of approximately 10 km at nadir, which degrades further towards the edges. Unlike the instruments discussed below, EPIC was not designed specifically for air quality monitoring, but rather to observe a broad range of Earth system properties, including clouds, aerosols, vegetation, and ozone, in addition to $SO_2$.

A further, more decisive step toward high-temporal-resolution air quality monitoring came with the development of dedicated geostationary satellites, forming the Geostationary Air Quality (GEO-AQ) constellation. Unlike EPIC, all three instruments in this constellation are hyperspectral grating spectrometers, purpose-built for atmospheric composition monitoring, providing continuous spectral coverage in the UV-visible range and enabling retrievals at hourly resolution over their respective regions. This constellation comprises GEMS, over East and Central Asia; TEMPO, over North America; and Sentinel-4, over Europe [Kim et al., 2020]. All three instruments provide hourly observations during daylight hours, while retaining a spatial resolution under 10 km.

Together with data from polar-orbiting satellites, these geostationary instruments are expected to substantially advance the understanding of the spatiotemporal distri-

bution of air pollutants, their emission sources, and their long-range transport [Kim et al., 2020].

The aim of this study is to evaluate the use of the GEMS $SO_2$ product for high-temporal-resolution estimation of $SO_2$ emission fluxes from Sakurajima Volcano. Sakurajima was selected as the target volcano because it is one of the most active volcanoes in Japan, characterised by near continuous degassing, and due to its location close to a densely populated region. This work focuses on a two-week period in November 2023, during which ground-based measurements from the Volcanic Emissions Observation and Modelling (VOLCOM) campaign were available for comparison. This work is structured around three objectives:

1. Estimate high temporal resolution $SO_2$ emission flux from Sakurajima using GEMS data.
2. Validate the resulting estimates against the ground-based measurements from VOLCOM campaign and Japan Meteorological Agency (JMA).
3. Assess the feasibility of reproducing the observed $SO_2$ plumes using the FLEXPART-WRF dispersion model, driven by the estimated $SO_2$ emission flux.

This study is structured as follows. Chapter 2 provides the theoretical background relevant to this study, covering $SO_2$ tropospheric chemistry, the DOAS method, $SO_2$ flux estimation, and atmospheric modelling. Chapter 3 presents the study area, the datasets and models used, and the details of the approach adopted in this study. Chapter 4 presents the results and discussion, and Chapter 5 provides the conclusions and an outlook.

# Chapter 2

# Theoretical background

This chapter presents the theoretical background relevant to this work. The first section describes the tropospheric chemistry of $SO_2$ and its end products. The second section introduces the fundamentals of the DOAS technique and how a gas vertical column density (VCD) can be retrieved from a spectral measurement. The third section presents different techniques for estimating emission fluxes, and the final section provides an introduction to atmospheric modelling.

## 2.1 Tropospheric $SO_2$

A major source of tropospheric $SO_2$ are anthropogenic emissions, primarily fossil fuel combustion and industrial activity, with an estimated global emission of 56.3 Tg(S)/yr. Natural sources contribute to a smaller share, dominated by volcanic emissions (6.6 Tg(S)/yr), with a further, smaller contribution from biomass burning (1.3 Tg(S)/yr) [Lee et al., 2011].

Once emitted, $SO_2$ can react in both the gas and aqueous phase, and is ultimately removed from the atmosphere via dry and wet deposition [Seinfeld and Pandis, 2016]

#### Gas-phase oxidation

In the gas phase, $SO_2$ is primarily oxidised by the hydroxyl radical (OH), ultimately producing sulfuric acid ($H_2SO_4$) through the following reaction sequence:

$$SO_2 + OH + M \longrightarrow HOSO_2 + M \tag{2.1}$$

$$HOSO_2 + O_2 \longrightarrow HO_2 + SO_3 \tag{2.2}$$

$$SO_3 + H_2O + M \longrightarrow H_2SO_4 + M \tag{2.3}$$

Here, $HOSO_2$ and $HO_2$ are reactive intermediate radicals, $SO_3$ is sulfur trioxide, and M represents a third body that absorbs excess energy to stabilize the reaction products, without itself being consumed in the reaction.

The resulting sulfuric acid can nucleate and condense to form sulfate aerosol particles, which contribute to increased concentrations of fine particulate matter ($PM_{2.5}$), which has well-documented negative effects on human health. These particles can subsequently be removed from the atmosphere via wet and dry deposition, producing acid deposition.

### Aqueous-phase oxidation

In the aqueous phase, $SO_2$ first dissolves into droplets, where it dissociates to form bisulfite ($HSO_3^-$):

$$SO_2(g) + H_2O \longleftrightarrow SO_2 \cdot H_2O \tag{2.4}$$

$$SO_2 \cdot H_2O \longleftrightarrow HSO_3^- + H^+ \tag{2.5}$$

$HSO_3^-$ can then be oxidised by either ozone ($O_3$) or hydrogen peroxide ($H_2O_2$), both of which are also taken up into the aqueous phase. Oxidation by $O_3$ proceeds as:

$$O_3(g) \longleftrightarrow O_3(aq) \tag{2.6}$$

$$HSO_3^- + O_3(aq) \longrightarrow HSO_4^- + O_2(aq) \tag{2.7}$$

$$HSO_4^- \longleftrightarrow SO_4^{2-} + H^+ \tag{2.8}$$

while oxidation by $H_2O_2$ proceeds as:

$$HSO_3^- + H_2O_2(aq) + H^+ \longrightarrow HSO_4^- + H_2O + H^+ \tag{2.9}$$

$$HSO_4^- \longleftrightarrow SO_4^{2-} + H^+ \tag{2.10}$$

where $H^+$ in Eq. 2.9 is acting as a catalyst for the reaction, therefore it is not net consumed.

Both pathways release $H^+$ ions, progressively acidifying the droplet. When droplets containing dissolved sulfate are removed from the atmosphere via wet deposition, this acidified water reaches the surface as acid rain.

### Atmospheric lifetime

The relative importance of gas- and aqueous-phase oxidation, together with removal by dry and wet deposition, determines the atmospheric lifetime of $SO_2$, which varies considerably with season and location. Lee et al. [2011] reported a lifetime inferred from in situ measurements of 19 ± 7 h in summer and 58 ± 20 h in winter.

## 2.2 Differential optical absorption spectroscopy

The Differential Optical Absorption Spectroscopy (DOAS) technique retrieves the amount of a trace gas from spectroscopic measurements of scattered or transmitted light, by exploiting the characteristic absorption features of that gas in a given spectral range. The theoretical framework presented in this section follows Platt and Stutz [2008].

The method is based on the Beer-Lambert law, which relates the intensity of light after passing through an absorbing medium to the concentration of the absorber along the light path:

$$I(\lambda) = I_0(\lambda) \cdot e^{-(\sigma(\lambda)\cdot\rho\cdot s)} \tag{2.11}$$

where $I_0$ is the incident intensity, $I$ the intensity measured at the detector after the light has passed through the absorbing medium, $\rho$ the concentration of the absorbing gas, $\sigma$ is the wavelenght dependent absorption cross section, and $s$ the length of the light path through the absorbing medium.

The light path is defined by the measurement geometry: for a satellite instrument, sunlight passes through the atmosphere and is scattered back toward the satellite by the Earth's surface and atmosphere. The effective path length therefore depends on both the solar zenith angle and the satellite viewing zenith angle, with larger angles corresponding to longer atmospheric paths and, consequently, stronger absorption.

What happens in the real atmosphere, however, is more complex than just absorption by one gas: multiple absorbing gases can contribute to the reduction in intensity at a given wavelength, and light is also scattered by air molecules and aerosols, known as Rayleigh and Mie scattering. Accounting for all these contributions, the Beer-Lambert law in Eq. 2.11 can be generalised as:

$$I(\lambda) = I_0(\lambda) \cdot \exp\left(-\sum_i \sigma_i(\lambda)\cdot\rho_i\cdot s - \sigma_{\text{Ray}}(\lambda)\cdot\rho_{\text{Ray}}\cdot s - \sigma_{\text{Mie}}(\lambda)\cdot\rho_{\text{Mie}}\cdot s\right) \tag{2.12}$$

where the the contribution of all gasses $i$ is summed up along the light path, and $\rho_{\text{Ray}}$ and $\rho_{\text{Mie}}$ represent the effective density of scatterers responsible for Rayleigh and Mie scattering, respectively.

Assuming the dependecy of the absorption cross section on the light path negligible, and defining the slant column density (SCD) of an absorber $i$ as its concentration integrated along the light path $s$:

$$\text{SCD}_\text{i} = \int \rho_i \, ds \tag{2.13}$$

Equation 2.12 can then be rewritten as:

$$I(\lambda) = I_0(\lambda) \cdot \exp\left(-\sum_i \sigma_i \cdot \mathrm{SCD}_i - \sigma_{\mathrm{Ray}} \cdot \mathrm{SCD}_{\mathrm{Ray}} - \sigma_{\mathrm{Mie}} \cdot \mathrm{SCD}_{\mathrm{Mie}}\right) \tag{2.14}$$

The method then separates the wavelength-dependent extinction coefficient into a slowly and a rapidly varying component, $\sigma'$ and $\sigma$ respectively. The rapidly varying component carries the characteristic information on the specific absorbing gas, while the slowly varying component arises from features that change smoothly with wavelength, such as instrumental effects and surface reflectance variations, and can be approximated by a polynomial. Since Rayleigh and Mie scattering also follow power-law dependencies on wavelength, their contribution can be combined with the slowly varying component and approximated by a single low-order polynomial. This allows Eq. 2.14 to be expressed in terms of the optical depth $\tau$, which constitutes the measured signal:

$$\tau = \ln\left(\frac{I_0(\lambda)}{I(\lambda)}\right) = \sum_i \sigma_i \cdot \mathrm{SCD}_i + \sum_p a_p \cdot \lambda^p \tag{2.15}$$

This yields a linear relationship between the optical depth and the SCDs of the absorbers of interest, which is solved via a linear least-squares fit within a selected spectral window.

The SCD obtained from this fit quantifies the absorber concentration integrated along the light path of a given measurement. This light path depends on viewing and illumination geometry, surface reflectivity, and the extent of atmospheric scattering and absorption along the lightpath — the latter influenced by factors such as aerosol loading, cloud cover, and the vertical distribution of the absorber itself. As a result, SCDs are not directly comparable, since the light path varies between measurements. To allow for meaningful comparisons across measurements, the SCD is converted into the vertical column density (VCD): the absorber concentration integrated along a purely vertical path through the atmosphere. This conversion is performed by dividing by an air mass factor (AMF), which accounts for all the dependencies mentioned above and is typically computed using a radiative transfer model.

$$\mathrm{VCD} = \frac{\mathrm{SCD}}{\mathrm{AMF}} \tag{2.16}$$

## 2.3 Methods for $SO_2$ flux estimation from satellite

Satellite retrievals provide the VCD of $SO_2$, expressed as an amount per unit area. To estimate the emission flux – an amount per unit time – this quantity must be combined with information on how the gas is transported and removed from the atmosphere.

Several methods have been developed for this purpose, differing in their underlying assumptions and in their input data.

All these methods rely on the principle of mass conservation: the amount of $SO_2$ observed at a given time reflects the balance between emission and loss. Losses can occur through chemical oxidation, in either the gas or aqueous phase (Section 2.1), through dry or wet deposition, or through transport and dilution of the plume below the satellite's detection limit. Regarding chemical loss, the kinetics of $SO_2$ is commonly approximated in the literature as a first-order process [Eatough et al., 1994].

Four main methods are used to estimate $SO_2$ emission flux from satellite observations [Theys et al., 2013].

### Box method

The box method is the simplest of the four. It defines a fixed area around a source and sums up the total $SO_2$ mass contained within it; this mass is then divided by the time required for the gas to reach the boundary of the box based on the wind field, yielding an estimate of the emission flux. A correction can be applied to account for the atmospheric lifetime of $SO_2$, allowing for chemical loss during the time the gas spends within the box.

### Cross-section (traverse) method

This method exploits the fact that, once emitted, $SO_2$ is transported downwind by the prevailing wind field. Under the assumption of a constant wind field, the wind speed and the distance from the source can be related to the plume's time of travel, allowing the flux to be calculated from the $SO_2$ mass crossing a transect placed at a given distance downwind. Transects placed farther from the source correspond to emissions released further back in time, so that a series of transects at increasing distances can, in principle, reconstruct a time series of past emissions. This relies on the assumption that the plume travels as a coherent unit in a single direction, and that the wind measured at the source is representative of the wind field along the entire plume. This method can achieve a high temporal resolution, limited only by the choice of transect position.

### Delta-M method

The Delta-M method is the only method that does not require knowledge of the wind field. It is based on the temporal change in the total $SO_2$ mass observed between successive satellite images, applying the mass conservation equation directly: the change in total mass over time equals the emission rate minus the loss rate.

#### Inverse modelling

Inverse modelling is the most complex of the four methods. It combines satellite VCD retrievals with an atmospheric transport model to reconstruct the emission height and timing that best reproduce the observed plume. This constitutes an ill-posed inverse problem, which must be solved using an optimal estimation approach.

Among these methods, the cross-section (traverse) method is adopted in this study, owing to its ability to provide flux estimates at high temporal resolution while relying only on wind field information.

## 2.4 Atmospheric modelling

Atmospheric modelling is used to represent the atmosphere, providing insight into processes that would otherwise be difficult or impossible to investigate through observations alone. Every model is a simplification of the real world, and therefore inherently imperfect; nonetheless, a model can be highly useful for studying a specific process or question [Seinfeld and Pandis, 2016].

Atmospheric models can be broadly divided into two main categories: Eulerian and Lagrangian frameworks.

### Eulerian models

In the Eulerian framework, the reference frame is fixed in space, and the atmosphere is observed as it moves through it. This is analogous to observing a fixed box and monitoring what enters, what exits, and what happens within it [Seinfeld and Pandis, 2016]. Eulerian models can be classified according to the number of spatial dimensions they resolve. In a 0-D model, no transport is represented at all, only processes occurring within a single box are considered, such as chemical transformations, emission, and deposition. A 1-D model can be thought of as multiple 0-D boxes stacked along a single direction, with transport allowed between them. This extends naturally to 2-D and 3-D models, which represent transport in two and three spatial dimensions, respectively.

To simulate the state of the atmosphere, a model solves a set of governing equations at each time step, yielding a set of prognostic variables (e.g., temperature, wind speed, and trace gas concentrations) that describe the atmospheric state and allow it to be propagated forward in time. From these prognostic variables, additional diagnostic variables can be derived (e.g., relative humidity, computed from temperature and water vapour content).

Some atmospheric processes cannot be explicitly resolved at any practical model resolution, despite playing an important role in determining the state of the atmo-

sphere. These processes must instead be represented through parameterisation. Common examples of parameterised processes include turbulent mixing within the planetary boundary layer and cloud microphysics.

A subset of Eulerian models is numerical weather prediction (NWP) models, such as the Weather Research and Forecasting (WRF) model, used in this study. Unlike general-purpose Eulerian transport models, NWP models are primarily designed to simulate atmospheric dynamics and physics – including wind, temperature, and moisture fields – rather than the transport of chemical tracers.

## Lagrangian models

In the Lagrangian framework, the reference frame follows an individual air parcel, tracking how its properties change as it moves through the atmosphere. The parcel's trajectory is governed by the equation of motion, to which diffusion, sedimentation, and other loss processes are subsequently applied [Lin et al., 2003].

Lagrangian models can be run in two modes, exploiting the time-reversibility of the underlying transport equations. In forward mode, particles are released at the source and their trajectories are run forward in time, so that the resulting particle distribution represents the dispersion of the emitted tracer. In backward mode, particles are released at the measurement location and their trajectories are run backward in time; the resulting particle density defines a footprint, representing the sensitivity of the measurement location to the potential emissions source.

# Chapter 3

# Methods

The methodology chapter is structured as follows. Section 3.1 presents the Sakurajima volcano. Section 3.2 introduces the datasets and models used throughout the study. Section 3.3.1 gives an overview of the overall workflow and finally Section 3.3.2 describes the cross-section method used to estimate $SO_2$ emission fluxes from GEMS data, including uncertainty calculation.

## 3.1 Study area

Sakurajima (peak height 1117 m) is located on Kyushu, the southernmost of Japan's main islands (31.577°N, 130.659°E; shown in Fig. 3.1a). It is one of the most active volcanoes in Japan, with approximately 80 eruptive events per month, in an area with high population density. Since 1995, its activity has shifted from large eruptive events to short-lived eruptive bursts, with an almost continuous background degassing from its vents [Poulidis et al., 2017; Poulidis and Iguchi, 2021]. As documented by the JMA, daily $SO_2$ emissions typically range between 1000 and 4000 t/day (Fig. 3.1c) [Japan Meteorological Agency, 2024]. Emitted plumes span heights from a few hundred metres to 5 km above sea level [Poulidis et al., 2017]. This persistent activity affects air quality not only in Kagoshima City but across the wider bay area, where the municipalities of Kagoshima, Kirishima, Kanoya, Aira, and Tarumizu (circled in black in Fig. 3.1b) are collectively home to approximately 900,000 inhabitants [Statistics Bureau, 2025]. This is one of the reasons the volcano is closely monitored by the JMA and has been the subject of the VOLCOM campaign (Section 3.2.2).

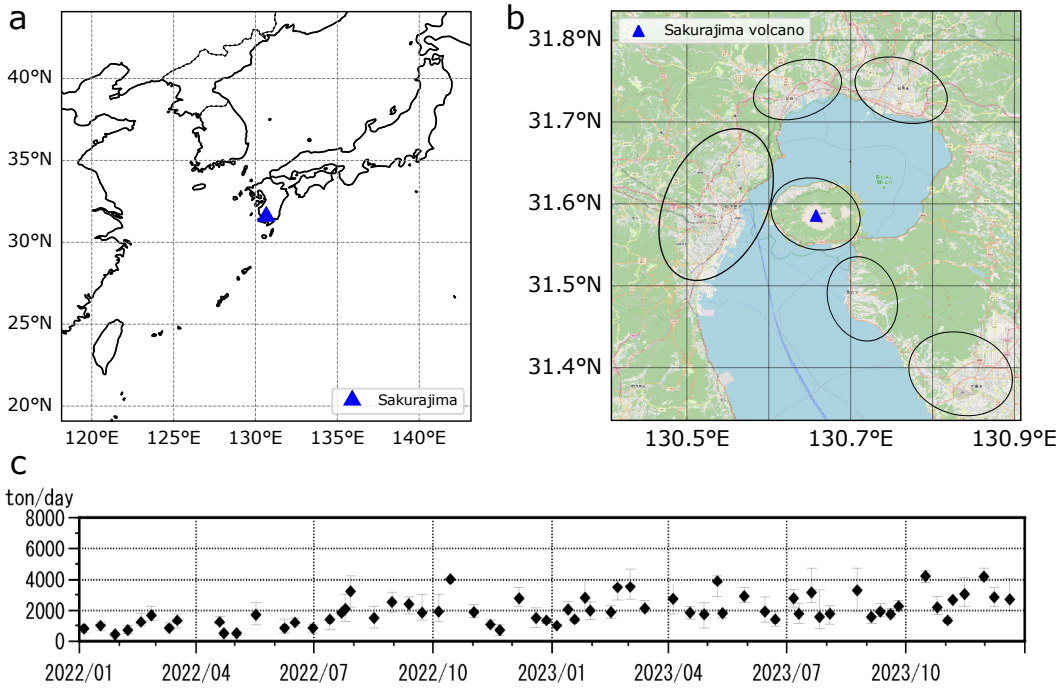



**Figure 3.1:** a) Location of Sakurajima volcano. b) Municipalities within the surrounding bay area (circled in black), home to approximately 900,000 inhabitants. c) Monthly $SO_2$ emissions reported by JMA. Panel (c) adapted from Japan Meteorological Agency [2024].

## 3.2 Datasets & models

### 3.2.1 Operational GEMS L2 $SO_2$ product v3.0.1

The Geostationary Environment Monitoring Spectrometer (GEMS) is a UV-visible grating imaging instrument, launched onboard the Geostationary Korea Multi-Purpose Satellite-2B (GEO-KOMPSAT-2B) in 2020. GEMS measures solar backscattered radiation from Earth's surface in the range of 300–500 nm, with a spectral resolution of 0.6 nm [Kim et al., 2020]. From these spectral measurements, information on several trace gases is retrieved at a spatial resolution of 7x8 $km^2$ at the reference position of Seoul, South Korea. Scans are performed using a step-and-stare method, combining a push-broom East-West setup with a scanning mirror [Seo et al., 2024]. GEMS monitors air quality over Asia, with a field of view spanning from East to Central Asia (5° S to 45° N in latitude and 75° E to 145° E in longitude).

In this study, the operational L2 $SO_2$ product v3.0.1, provided by the Environmental Satellite Center (ESC) of the National Institute of Environmental Research (NIER), Republic of Korea, is used. The data are freely available from ESC [ESC]. To increase the signal-to-noise ratio of the $SO_2$ product, two pixels are binned together, reducing the spatial resolution to 7x16 $km^2$. The retrieval algorithm combines the DOAS technique with Principal Component Analysis [Kim et al., 2020].

During the study period (November 2023), Sakurajima fell within the scanning region during six scans per day, from 00:45 to 05:45 UTC (times relative to scan start), corresponding to a nominal temporal resolution of 1 h. In this work, scans are identified by the hour at which they started, used as an index relative to the scan (00, 01, 02, 03, 04, 05, respectively). The period analysed covers two weeks in November, from the 3rd to the 16th, corresponding to the VOLCOM campaign period (Section 3.2.2).

It should be noted that, to maximise coverage of its field of view, GEMS does not scan a fixed spatial pattern at fixed times, but rather adjusts its pointing over the course of the day: in the early morning, the instrument points further east, following sunrise, and progressively shifts westward as the day proceeds. As a result, the exact revisit time for a given pixel varies slightly depending on its position within the scanning domain, rather than following the nominal 1-hour interval. For example, during the period analysed in this study, a pixel over Sakurajima was scanned at 01:06 in the morning, but by the last scan of the day it was scanned at 05:46 rather than 06:06, corresponding to a 20-minute shift between the first and last scan of the day.

### 3.2.2 VOLCOM campaign

The VOLCOM campaign [Poulidis et al., 2023] was conducted around Sakurajima volcano (see Section 3.1) from November 3rd to November 16th of 2023, as part of an international collaboration studying the transport of emissions from small eruptions and volcanic degassing. The campaign's main objective was to test the capability of a plume-forecasting model developed at IUP Bremen to predict the location of the volcanic plume [Poulidis et al., 2023]. The campaign combined two DOAS instruments: a stationary system installed at the Kurokami station, and a car system operated while driving around and near the volcano. Both instruments performed zenith-sky DOAS measurements, focusing on the retrieval of two species, BrO and $SO_2$.

Ground-based fluxes were calculated using the traverse method [Galle et al., 2010]. In this approach, the flux is calculated through a surface corresponding to a full circle around the source. Most drives consisted of a complete circle around the volcano; in some cases, however, only part of the circle was covered (example routes are shown in Fig. 3.2). In these cases, the flux through the uncovered portion of the circle was assumed to be negligible.

In this study, the $SO_2$ flux dataset is used as an independent ground-based dataset to evaluate the fluxes obtained from the GEMS product (Section 4.2). The fluxes were originally calculated in t/s and were converted to t/h to allow direct comparison with the GEMS-derived estimates.

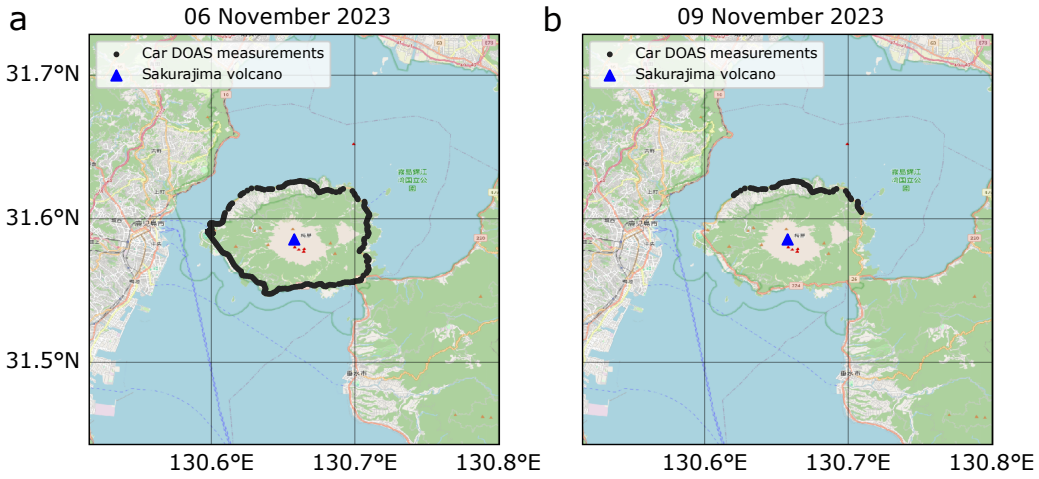



**Figure 3.2:** Example driving routes of the VOLCOM campaign. a) Complete circle around the volcano. b) Route covering only part of the circle.

### 3.2.3 JMA $SO_2$ flux

The Japan Meteorological Agency (JMA) monitors Sakurajima volcano and publishes monthly activity reports, summarising, among other parameters, the $SO_2$ emission rate of the volcano. On days with suitable weather conditions, the agency performs traverse DOAS measurements and then calculates the flux similarly to the VOLCOM campaign. Measurements are carried out at irregular intervals, typically one or three times per month [Iguchi et al., 2022].

For each measurement day, only the mean $SO_2$ emission rate is reported, together with the minimum and maximum values recorded. During the period analysed in this study, two measurement days are available: 6 November, with a mean $SO_2$ emission flux of 2700 t/day (range: 2600–2800 t/day), and 15 November, with a mean $SO_2$ emission flux of 3000 t/day (range: 2700–3600 t/day) [Japan Meteorological Agency, 2024]. These daily emission values were converted into t/h by dividing by 24, and were assumed to be representative of a constant emission rate throughout the entire day.

This dataset is also used to evaluate the $SO_2$ emission flux estimates obtained from the GEMS product (Section 4.2), providing an additional, independent ground-based reference against which the satellite-derived emission rates can be compared.

### 3.2.4 ERA5 reanalysis

ERA5 is a global atmospheric reanalysis product produced by the European Centre for Medium-Range Weather Forecasts (ECMWF). It combines various observational datasets with a meteorological forecast model to produce a physically consistent representation of the atmosphere in space and time. It has a spatial resolution of $0.25° \times 0.25°$ in latitude and longitude, 137 hybrid sigma levels in the vertical (top level at 0.01 hPa),

and an hourly output, providing a large number of output variables [Hersbach et al., 2020; European Centre for Medium-Range Weather Forecasts]. Wind information is provided as zonal and meridional components, from which wind speed and direction are derived and used in the cross-section method (Section 3.3.2) to estimate the $SO_2$ flux. ERA5 output is also used to initialise the regional Weather Research and Forecasting (WRF) model, described in the following section.

### 3.2.5 WRF regional model

The first model used in this study is the Weather Research and Forecasting (WRF) model, version 4.5 [Skamarock et al., 2019]. WRF is a model used for regional-scale studies and was used here to downscale the ERA5 reanalysis data by means of nested domains. It is a three-dimensional, non-hydrostatic model that solves the governing equations in flux form within an Eulerian framework.

The possibility of achieving high resolution with this model was what made it suitable for this study. The output of this model was then used as input data for FLEXPART-WRF (Section 3.2.6).

The simulation covered the period from 26 October to 17 November 2023 and was performed using ERA5 data as boundary conditions, with five one-way nested domains (Fig. 3.3) and 88 vertical eta levels, with the model top set at 50 hPa. In order to keep the large-scale flow closer to the ERA5 input data while allowing smaller-scale features to develop freely in the simulation, spectral nudging was applied to the outermost domain (domain 1) with a time step of one hour [Miguez-Macho et al., 2004]. It targeted the horizontal wind components, temperature, water vapor mixing ratio, and geopotential height, each with the nudging coefficient of 0.0003. A cutoff wavenumber of 4 was used in both the x and y directions, corresponding to a cutoff wavelength of approximately 1000 km.

The first domain covers a large part of northeastern Asia (grid spacing $\Delta x = \Delta y =$ 30 km, 150 $\times$ 150 grid points); the second is centred over southern Japan and Korea (grid spacing $\Delta x = \Delta y = 10$ km, 151 $\times$ 151 grid points); the third covers Kyushu (grid spacing $\Delta x = \Delta y = 3.3$ km, 172 $\times$ 172 grid points); the fourth covers the southern half of Kyushu (grid spacing $\Delta x = \Delta y = 1.1$ km, 235 $\times$ 319 grid points); and the fifth covers Kagoshima Prefecture (grid spacing $\Delta x = \Delta y = 0.37$ km, 388 $\times$ 337 grid points). Model output was saved every 15 minutes, in order to obtain high temporal as well as spatial resolution.

The time steps of the computation were initially set to 90, 30, 10, 3.3, and 1.1 s for the five domains, respectively. Due to specific conditions on 9 November 2023, the time steps were reduced to avoid segmentation errors; from that point onward, the time steps for the five domains were set to 90, 10, 3.3, 3.3, and 1.1 s. A further adjustment

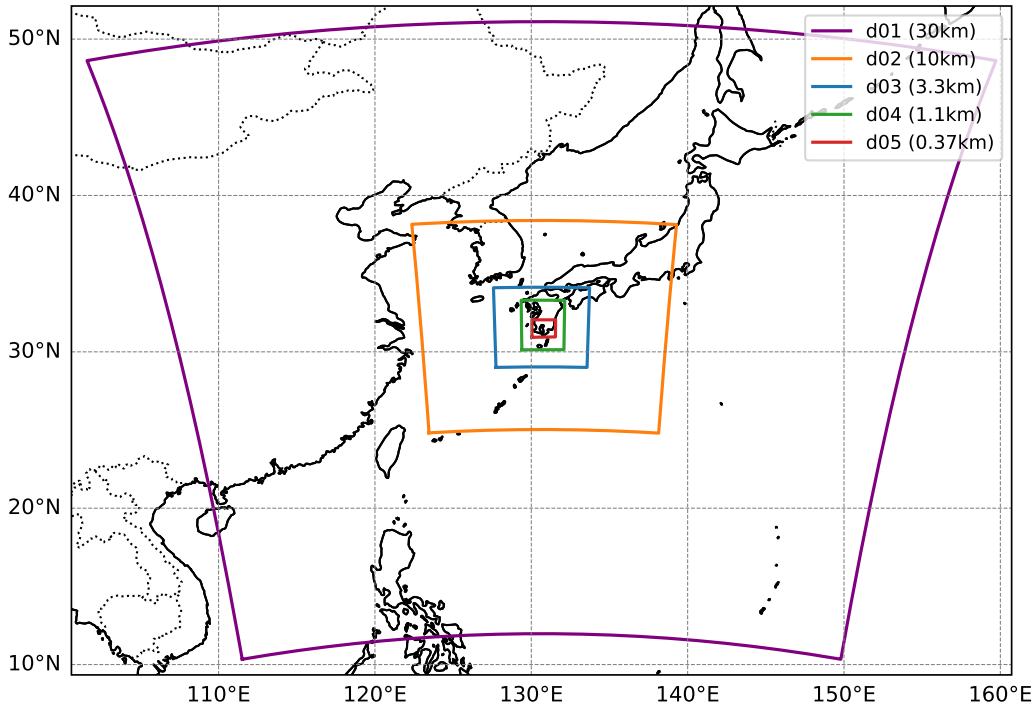



**Figure 3.3:** WRF nested domains configuration.

was made on 10 November 2023, when the time steps were set to 60, 20, 6.7, 2.2, and 1.1 s.

The physical parametrizations used in the WRF simulations are summarized as follows. Microphysical processes were represented using the WRF Single-Moment 5-class (WSM5) scheme [Hong et al., 2004], while cumulus convection was parameterized using the Kain–Fritsch scheme [Kain, 2004]. The latter was applied only to domains 1 and 2, since in the finer domains (3–5), where the grid spacing is 3.3 km or less, convection is resolved explicitly by the model rather than parametrized. For radiative transfer, the Rapid Radiative Transfer Model (RRTM) [Mlawer et al., 1997] was used for longwave radiation, and the Goddard scheme [Chou and Suarez, 1994; Matsui et al., 2020] for shortwave radiation. The planetary boundary layer was represented using the Shin–Hong scheme [Shin and Hong, 2015], in combination with the Revised MM5 surface layer scheme [Jiménez et al., 2012], and land-surface processes were parametrized using the 5-layer thermal diffusion scheme [Dudhia, 1996], applied across all five domains.

### 3.2.6 FLEXPART-WRF model

The second model used in this study is the FLEXible PARTicle dispersion model v3.1 driven by WRF (FLEXPART-WRF) [Brioude et al., 2013]. FLEXPART is a Lagrangian particle dispersion model designed to simulate a wide range of atmospheric transport processes, including advection and turbulent diffusion, dry and wet deposition, radioactive decay, and linear chemistry. It can be run in forward mode, dispersing

from a point source, or in backward mode, to identify possible sources, and it is applicable across scales ranging from local to global. FLEXPART-WRF is a variant of the model that uses meteorological fields from the WRF model as input, allowing simulations at a finer spatial and temporal resolution than the coarser global reanalysis products used by the standard FLEXPART model.

In this study, FLEXPART-WRF was driven by the WRF simulation described in Section 3.2.5, using output from domains 4 and 5, corresponding to horizontal resolutions of 1.1 km and 0.4 km, respectively, with meteorological fields provided at 15-minute intervals. The FLEXPART-WRF simulation domain extended from 129.4° to 132.0°E in longitude and from 30.2° to 33.2°N in latitude, with a vertical extent of up to 20 km. The trajectory output of the model was used in this analysis, with dry and wet deposition included in the simulations. Chemical transformation and radioactive decay were not included: this simplification is justified by the short simulation duration (12 h) relative to the atmospheric lifetime of $SO_2$ in the troposphere, which is on the order of days (Section 2.1).

For each hour of the study period, a separate 12 h forward simulation was performed (372 simulations in total), with an emission duration of 1 h at the start of each run, released from a point source located at the coordinates of the volcano. Since the injection height of the emitted $SO_2$ was not known a priori, the emission was distributed over 20 discrete release-height intervals spanning 0–3000 m at 150 m vertical resolution. Each height interval was assigned a separate tracer, so that the contribution from each release height could be tracked independently throughout the simulation. Each tracer was released with a unit mass, such that the resulting particle mass fractions at any later time directly represent the percentage of the initially emitted mass. Each release height was represented by 100,000 parcels, and a parcel splitting time of 15 min was used to maintain a smooth and well-resolved representation of the plume in space. the model output was saved at 1 h intervals.

The resulting simulated trajectories were post-processed to derive a modelled $SO_2$ VCD, which was then compared to the $SO_2$ VCD retrieved from GEMS (Section 4.2).

## 3.3 Analytical framework

### 3.3.1 Overview of the work

The workflow of this study is structured around three main steps. First, $SO_2$ emission fluxes are estimated using the cross-section method applied to the VCD from the GEMS product. Since the cross-section method requires wind fields as input, data from the ERA5 reanalysis product are used in this study. The uncertainty associated with this

estimate is then quantified, accounting for the main sources of error in the method: wind speed, plume height, and GEMS retrieval uncertainty (Section 3.3.2.1).

Second, the resulting $SO_2$ emission estimates are evaluated against independent ground-based measurements from the VOLCOM campaign and from the JMA, to assess the capability of the cross-section method when applied to the GEMS product.

Finally, the $SO_2$ emission rates are used as initial conditions in FLEXPART-WRF dispersion simulations. The modelled $SO_2$ plume is then compared to the GEMS product, providing a means of assessing whether the estimated emissions in combination with transport modelling are able to reproduce the observed distribution of $SO_2$.

### 3.3.2 Cross-section method

The cross-section method is used to estimate the emission rate of a gas from a point source, using measurements of its plume together with wind information. The method exploits the fact that, once emitted, the gas is transported downwind by the wind field, forming an elongated plume whose orientation and extent are determined by wind direction and speed. To estimate the emission flux, transects – straight lines perpendicular to the wind direction – are drawn across the plume at increasing distances downwind of the source, and the $SO_2$ mass contained between two consecutive transects is used to calculate the flux for that section of the plume.

This procedure can be expressed mathematically, as shown in Merucci et al. [2011]:

$$F = \left( \sum_i \mathrm{VCD}_i \cdot x_i \right) \cdot v \cdot \cos(\alpha) \tag{3.1}$$

where $\mathrm{VCD}_i$ is the vertical column density at pixel $i$ along the transect, $x_i$ is the pixel size (or spacing) along the transect, $v$ is the plume transport speed, and $\alpha$ is the angle between the wind direction and the transect orientation.

In this study, transects are drawn perpendicular to the wind direction by construction (Section 4.1.2), so that $\cos(\alpha) = 1$. Furthermore, since transects are spaced according to the wind speed and a fixed time interval of 1 h (Section 4.1.2), the flux can equivalently be expressed as:

$$F = \frac{M}{\Delta t} \tag{3.2}$$

where $M = \sum_i \mathrm{VCD}_i \cdot Area_i$ is the total $SO_2$ mass contained between two consecutive transects, and $\Delta t$ is the fixed 1-hour interval corresponding to the plume travel time between them.

Since this travel time is directly related to the distance from the source via the wind speed, transects placed farther downwind correspond to emissions released further back in time. As a result, a single scan can provide emission estimates for several hours prior

to the scan time, extending the temporal coverage beyond that of the individual GEMS scans alone, and yielding a sub-daily resolution of the $SO_2$ emission estimates.

The cross-section method relies on three main simplifications. Firstly, the plume is treated as a two-dimensional shape with no vertical extent, lying on a single horizontal plane at a fixed height. Secondly, for the choice of the wind, a single wind vector — taken at the volcano location, at the assumed plume height — is used to define the transport direction and speed for the entire plume, corresponding to passive advection of the gas in a constant wind field [Theys et al., 2013]. This second assumption implies that the wind field is approximately homogeneous over the plume's spatial and temporal extent, which usually is not strictly true: emissions released earlier in time have been transported under atmospheric conditions that may differ from those at the scan time, and this discrepancy grows the further back in time an emission occurred. As a result, the assumption introduces additional uncertainties, particularly for transects located far downwind. Wind-related uncertainty is generally recognised as the dominant source of error in flux estimates obtained with the cross-section method [Theys et al., 2019]. Thirdly, no loss of $SO_2$ within the plume is assumed. This is justified because $SO_2$ has a tropospheric lifetime of the order of a few days (Section 2.1), whereas the plume analysed here has a lifetime of only a few hours before being diluted or transported out of the domain. Assuming a lifetime of 58 h [Lee et al., 2011] and a first-order loss process [Eatough et al., 1994], this corresponds to a loss of approximately 7% of the $SO_2$ mass after 4 h, which is considered a minimal correction and is therefore neglected.

The method is applied in two steps. First, the GEMS product are screened to select those on which a plume can be identified, discarding $SO_2$ data affected by excessive noise in the region of the volcano or by unstable wind conditions (Section 4.1.1). Second, for each selected scan, transects are drawn and the corresponding emission fluxes are calculated (Section 4.1.2).

Since transects are spaced at 1-hour intervals, matching the nominal hourly interval between GEMS scans (Section 3.2.1), the first transect (the one nearest to the volcano) of a scan at time $N$ corresponds approximately to the same emission time as the second transect of the scan at time $N+1$ h, and so on for later transects. As a result, multiple scans can provide independent flux estimates for approximately the same point in time. However, as discussed in Section 3.2.1, the exact scan time over Sakurajima varies slightly from one scan to the next, due to the progressive westward shift of the GEMS field of view; consequently, the emission times derived from different scans do not align exactly.

To obtain a single hourly emission estimate, flux values originating from different scans, with emission times within 30 minutes of each other, were grouped together and averaged, with the associated uncertainty propagated accordingly.

#### 3.3.2.1 Uncertainty quantification

The emission flux estimates obtained with the cross-section method are affected by several sources of uncertainty. In this study, three main contributions are considered: the uncertainty associated with wind speed, the uncertainty associated with the choice of plume height, and the retrieval uncertainty of the $SO_2$ GEMS product itself. Each of these sources is quantified independently, and the resulting uncertainties are then combined to obtain an overall estimate of the flux uncertainty 3.3.

The first source considered is the uncertainty in wind speed, arising from the ERA5 wind field used in the flux calculation. To quantify this uncertainty, a perturbation approach is applied: the wind speed used in the flux estimation is perturbed by $\pm 0.5$ m/s, and the flux is recalculated accordingly. Since the flux is linearly dependent on wind speed, this perturbation propagates directly into a corresponding change in the estimated flux. The resulting spread in the flux estimates is taken as the wind-speed-related uncertainty, $\sigma_v$.

The second source is the uncertainty associated with the choice of plume height. This choice affects the flux estimate in two ways: it determines the wind speed and direction used in the calculation, since both vary with altitude, and it defines the orientation of the transects, which are drawn perpendicular to the wind direction. As a result, an incorrect plume height can affect not only the magnitude of the transported flux but also the geometry used to compute it. Following the same perturbation approach used for wind speed, the plume height is varied by $\pm 100$ m around the assumed value, and the flux is recalculated for each case, giving $F_-$ and $F_+$. The absolute differences between the original flux and $F_+$, and between the original flux and $F_-$, are then computed, and their mean is taken as the plume-height-related uncertainty, $\sigma_h$.

The third source of uncertainty considered is the retrieval uncertainty of the GEMS $SO_2$ VCD product, $\sigma_{\mathrm{VCD}}$. Since a comprehensive validation of the product is not yet available, a fixed value of $1 \times 10^{16}$ molecules/cm$^2$ is assumed, following Kim et al. [2020].

The three sources of uncertainty are assumed to be independent of one another, since they originate from unrelated aspects of the measurement and modelling chain. Under this assumption, the total uncertainty in the flux estimate, $\sigma_{\mathrm{tot}}$, is obtained as the quadrature sum of the individual contributions:

$$\sigma_{tot} = \sqrt{\sigma_v^2 + \sigma_h^2 + \sigma_{VCD}^2} \tag{3.3}$$

# Chapter 4

# Results & discussion

This chapter presents the results of the study. It begins with the outcomes of the plume selection procedure applied to the $SO_2$ VCD L2 GEMS product, followed by the resulting $SO_2$ emission rate estimates, including uncertainty estimations. These estimates are then compared against ground-based measurements from VOLCOM and JMA to assess the level of agreement. Finally, using the estimated emissions as input, the $SO_2$ plume is simulated with the FLEXPART-WRF dispersion model and compared against the GEMS product to evaluate how well the estimated emission reproduce the observed $SO_2$ distribution.

## 4.1 Application of the cross-section method to GEMS retrieval

### 4.1.1 Plume identification

To identify a plume in the scans of GEMS product, a series of conditions and exclusion criteria were applied, which are described in the following. This procedure is illustrated using one example scan from 14 November 2023 scan 00. Following Theys et al. [2019], the analysed area was restricted to a 3°×3° box centred on the volcano, typically containing between 1000 and 1200 pixels (Fig. 4.1a), and pixels within this box exceeding a threshold of |1 DU| were selected (Fig. 4.1b, grey). In this study, several additional criteria were then applied. Only pixels with at least one neighbouring pixel also exceeding this threshold were retained (Fig. 4.1c, green); the rest were considered noise. Neighbouring pixels were defined using an 8-connectivity scheme (up, down, left, right, and the four diagonals). This resulted in several distinct groups of connected pixels, among which only those containing at least 50 t of $SO_2$ were considered possible plumes (Fig. 4.1d, blue, 'Big groups'). If multiple candidate groups met this criterion, the $SO_2$-mass-weighted centre of mass of each group was calculated, and the group

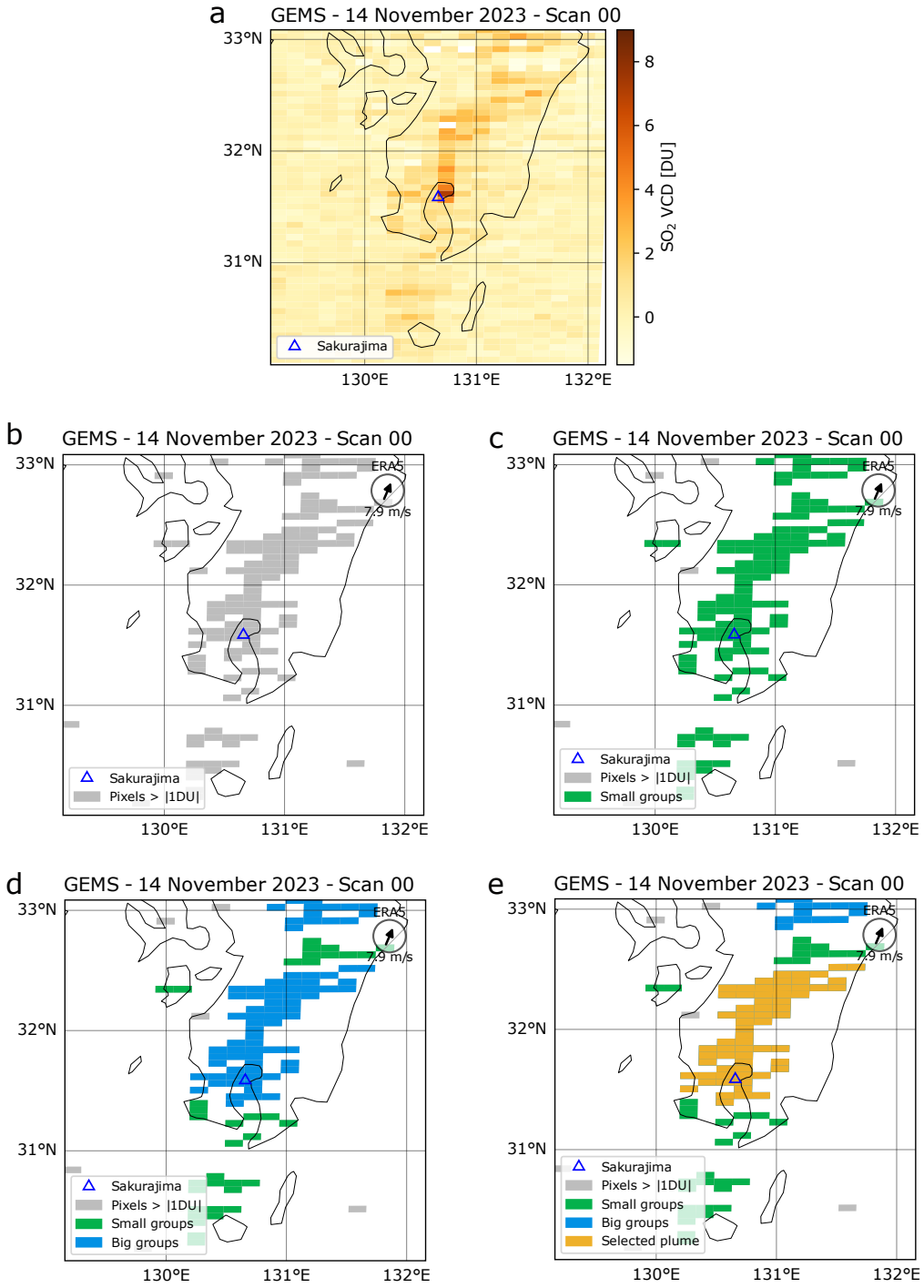



**Figure 4.1:** Plume selection method. a) GEMS $SO_2$ VCD L2 product. b) Pixels with $SO_2$ VCD > |1 DU|. c) Pixels with at least one neighbouring pixel also exceeding the threshold. d) Pixel groups containing at least 50 t of $SO_2$. e) Pixel group closest to the volcano.

closest to the volcano was selected (Fig. 4.1e, orange); proximity to the source implies a shorter time since emission, therefore lower uncertainty. If no pixel group reached the 50 t threshold, no plume could be defined, and the scan was discarded.

In the GEMS product (Fig. 4.1a), a plume is visible, with its highest $SO_2$ concentration, around 7 DU, located directly above the volcanic vent. The plume extends toward the north/north-east, with concentrations gradually decreasing along its length and fading toward the edges as the plume diffuses into the surrounding background. Outside the plume, scattered pixels above the |1 DU| threshold are also present across the analysed box, reflecting retrieval noise rather than volcanic signal. Applying the neighbouring-pixel and weighted-centre-of-mass criteria removes most of this noise, isolating a single coherent group of pixels that matches well the plume visible in the GEMS retrieval (Fig. 4.1e, orange).

Having identified the plume's spatial extent, the next step is to determine the wind field driving its transport. As described in Section 3.3.2, the cross-section method assumes the plume lies on a single horizontal plane. To define the height of this plane, the ERA5 output closest to the Sakurajima scan time was selected, and its vertical coordinate was converted from hybrid sigma levels to height above ground. The wind vectors over the volcano were then scanned from 0 m to 5000 m, at intervals of 50 m, and the wind vector whose direction was closest to the direction of the $SO_2$-mass-weighted centre of mass of the plume was selected to define the transport direction and wind speed of the entire plume; the height of this wind vector was taken as the plume height.

In addition to these selection criteria, two exclusion criteria were applied to ensure the quality of the selected scene:

- Noise criteria: once a plume has been identified, all pixels exceeding the |1 DU| threshold that did not belong to the plume were counted and considered noise. If this count exceeded a noise threshold of 105 pixels, the scene was considered too noisy, and the scan was excluded from the analysis. An example of such a situation is presented in Fig. 4.2.

- Unstable wind criteria:If the plume was subject to a highly variable wind field, this could introduce instability in the plume's shape and transport. In such cases, the scan was discarded, as a constant wind field is one of the underlying assumptions of the cross-section method. To quantify wind-field variability, the ERA5 wind field at the plume height was extracted, and all wind vectors overlapping the selected plume were identified (Fig. 4.3b, orange arrows). The standard deviation of the wind-vector directions was then calculated as a measure of the spatial variability of the wind field (Fig. 4.3c). An exclusion threshold of 40° was

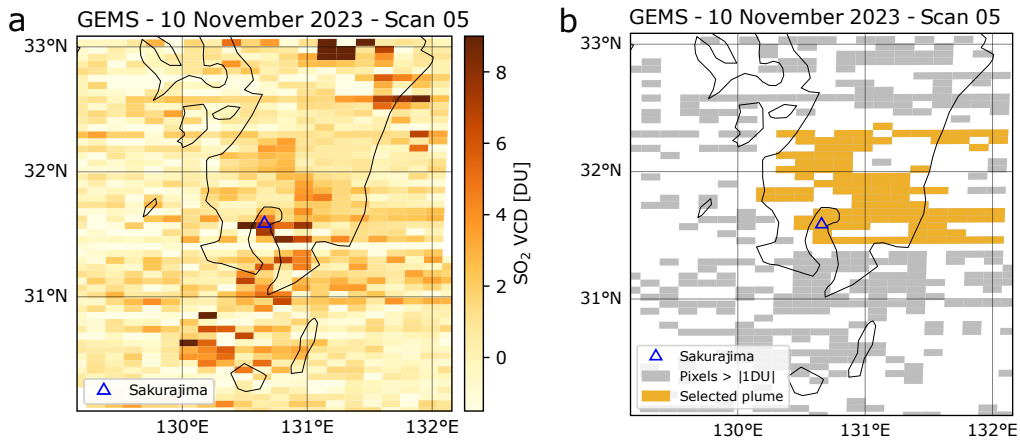



**Figure 4.2:** a) GEMS product. b) Noise criteria example.

determined empirically (dashed line). Applying this criterion resulted in the exclusion of two scans. One of these is shown as an example in Fig. 4.3b, where the wind vectors associated with the plume exhibit substantial directional scatter.

Overall, the dataset started with 84 scans, of which 41 remained after applying the plume-selection procedure. The next step was to draw transects across the identified plume and calculate the corresponding $SO_2$ emissions.

### 4.1.2 Transects definition

The wind vector selected from ERA5 fields was projected onto the geographic coordinate system (latitude-longitude), and the transport axis was drawn parallel to the wind direction, passing through Sakurajima (Fig. 4.4a, black line).

The transverse direction was defined as perpendicular to this axis (Fig. 4.4, solid green line). Transects were then drawn parallel to the transverse direction at 1-hour intervals, with the spacing between them determined by the wind speed (Fig. 4.4, dashed green lines). The mass of $SO_2$ present between two consecutive transects was summed and divided by the time required for the plume to travel between them – 1 hour, by construction – yielding the $SO_2$ flux, or emission rate, for that segment of the plume.

As a result, each transect provides an emission estimate representative of 1 hour, starting from the scan time over Sakurajima and for time in the past. Any plume pixels located upwind of the source would imply an emission occurring in the future, which is unphysical; these pixels were therefore assigned to the first transect, the one closest to the volcano, since the more reasonable interpretation is that this $SO_2$ was emitted only shortly before the scan time (Fig. 4.4, light blue pixels).

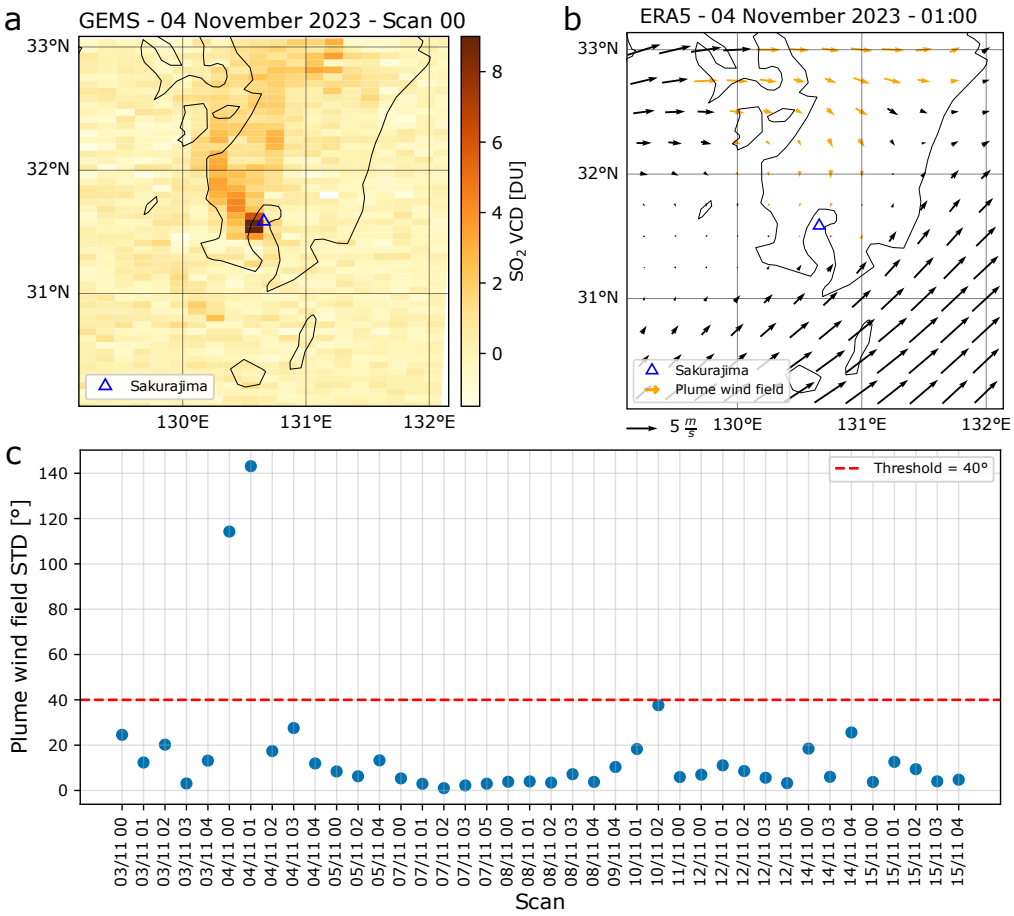



**Figure 4.3:** Unstable wind criteria. a) GEMS product. b) ERA5 wind field; in orange, the wind vectors overlapping the plume. c) Standard deviation of the plume wind field direction for each scan. Dotted line is the exclusion threshold. The x-axis is the identification of each scan.

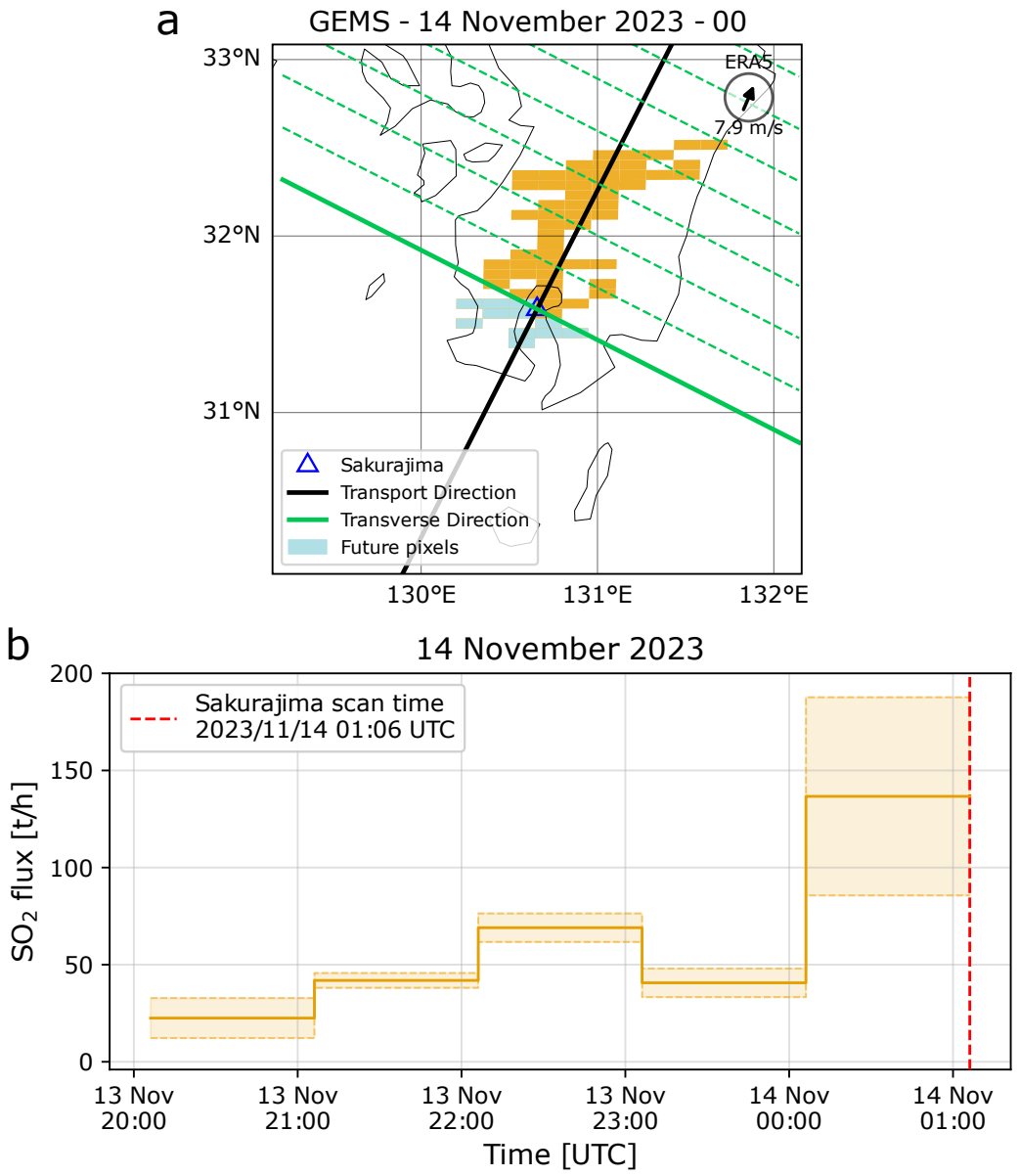



**Figure 4.4:** Transects definition. a) In orange, the selected plume. In light blue, pixels upwind of the volcano, included in the first transect. In black, the transport direction. In solid green, the transverse axis; in dashed green, the subsequent transects drawn downwind parallel to the transverse direction. In the top right, the ERA5 wind vector used for the scan. b) Example of the resulting $SO_2$ emission flux estimates for each transect, as a function of time before the scan; the shaded area represents the total uncertainty.

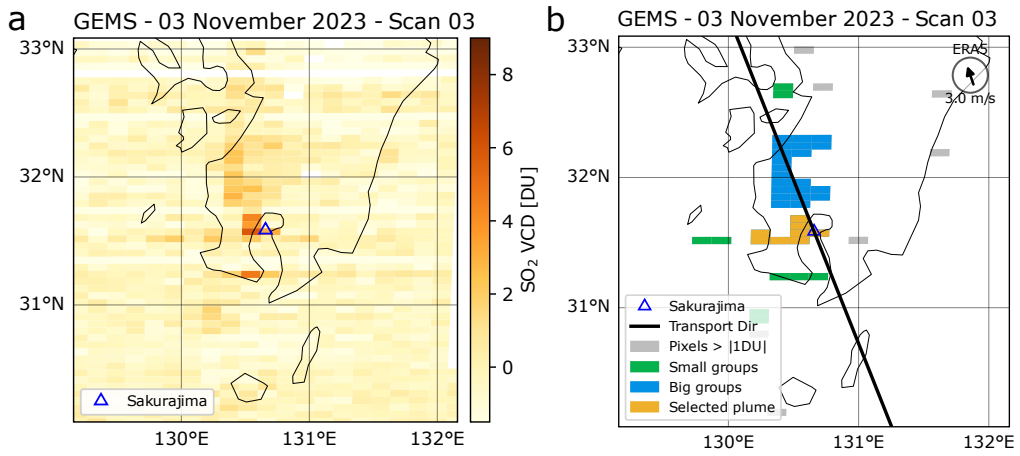



**Figure 4.5:** Plume selection problem - discontinuous plume. a) GEMS product. b) Plume selection.

Fig. 4.4b presents the final flux estimates for the example scan. The x-axis represents time, moving backward from the scan time over Sakurajima; each step on the plot corresponds to the emission flux estimated from one transect, at hourly intervals into the past. The shaded area represents the total uncertainty, arising from the propagation of uncertainty in plume height, wind speed, and GEMS VCD retrieval, as described in Section 3.3.2.1. For this example scan, the estimated $SO_2$ flux is 140 t/h at the scan time. Moving backward in time, the flux shows a decreasing trend, reaching a minimum of 20 t/h. This temporal evolution is consistent with the spatial distribution of the plume (Fig. 4.1a), where the bulk of the $SO_2$ mass is concentrated close to the volcano.

These scenes were then visually inspected to check the quality of the selection. Most days show a plume, which could then be observed being transported away over the course of the later scans of the day.

One observed problem is that the selection algorithm allows for only one plume to be selected at a time. However, one possible scenario in volcanic degassing is that the volcano emits, pauses briefly, and then emits again, resulting in two separated plumes. This was observed in four scans within the analysed period. Fig. 4.5 is an example of such a case, where the blue pixel group is likely to part of the plume.

An additional criterion could therefore be introduced: once the main plume has been selected, pixel groups lying along the same axis could also be included in the calculation. Without this feature, it is likely that emission fluxes were underestimated on some days.

A further limitation of the selection algorithm was observed in one scan, where the selected plume was likely a retrieval artefact rather than a genuine volcanic plume

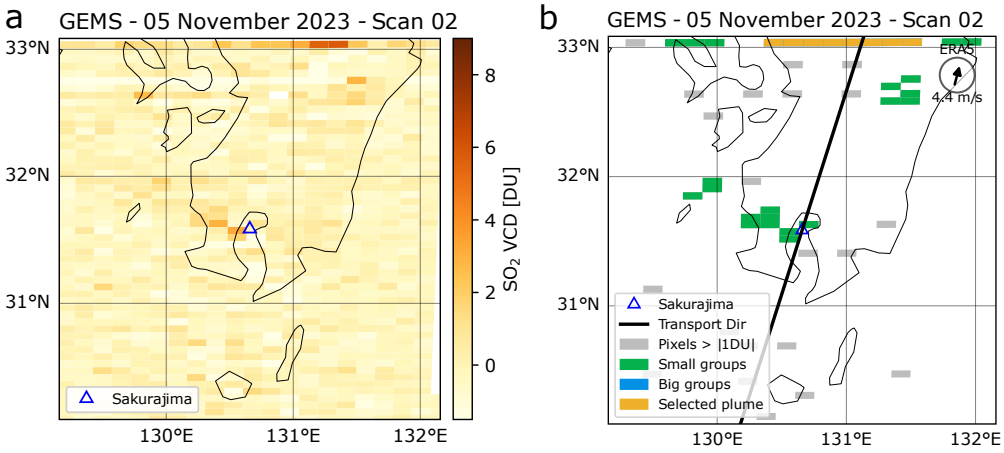



**Figure 4.6:** Plume selection problem - artefact. a) GEMS product. b) Plume selection.

(Fig. 4.6). Additional exclusion criteria – for example, excluding plumes with an unusually regular geometric shape – would help prevent such cases from being misidentified.

### 4.1.3 $SO_2$ flux estimation

One advantage of the hourly GEMS observations is that multiple scans can provide independent emission estimates for the same hour. These estimates can therefore be directly compared, providing a useful check on the consistency and robustness of the method. Flux estimates were calculated for all scans that passed the selection procedure and are presented per day, showing, where available, multiple estimates for the same hour.

Of the 14 days analysed, 11 passed the selection procedure. For some days, only one or two scans were retained, and in some cases no temporal overlap could be found between scans, as the identified plume was not sufficiently extended. Of these 11 days, five (3rd, 4th, 8th, 14th, and 15th November) had multiple scans with substantial temporal overlap, allowing the temporal trend to be examined.

Across all days, estimated fluxes range from near-zero, during quiescent moments, to approximately 100 t/h, with occasional higher values reaching a maximum of 200 t/h on the 10th of November. This maximum value was investigated further and found to result from a large number of pixels located upwind of the source (i.e., on the "future" side of the transects). As described in Section 4.1.2, all such pixels are assigned to the first transect, which can lead to an overestimation of the flux from the first transect. This may in turn correspond to an underestimation of the flux at an earlier transect, if the $SO_2$ in question was in fact emitted several hours prior – for instance, at a different plume height which is not well represented by the single wind vector used in

the analysis. Addressing this limitation would require identifying multiple plumes and plume heights within a single scan, which is left for future work.

A similar limitation can occur for the last transect of the plume, when the transect is located close to the edge of the analysis domain. In such cases, part of the plume may extend beyond the domain boundary and therefore remain outside the area considered in the analysis. As a result, a portion of the plume may not be captured, potentially leading to an underestimation of the corresponding emission flux. Although this occurred only occasionally, the resulting flux estimates should therefore be considered potentially lower than the true emissions.

As an example, results for 14 November 2023 are presented in Fig. 4.7; the individual per-scan flux estimates for all other days are shown in Appendix A.1.

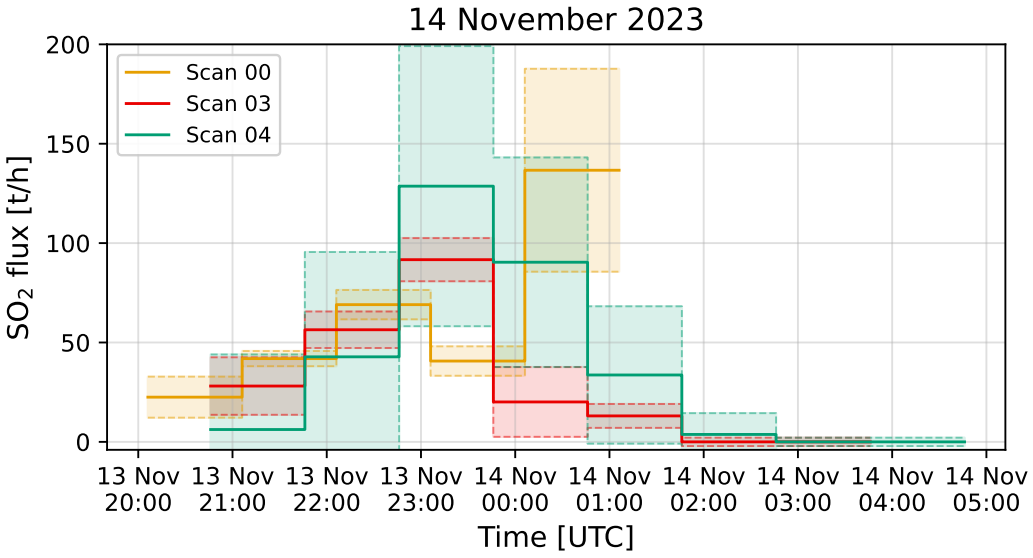



**Figure 4.7:** $SO_2$ flux estimations from 3 scans (coloured lines) on the day 14 November 2023. The shadow is the uncertainty.

For this example, the three scans show comparable flux values, ranging between 0 and approximately 100–140 t/h. Scans 03 and 04 agree particularly well with one another, both showing a distinct bell-shaped curve: starting from a low emission of approximately 20 t/h in the evening of the 13th, rising to a peak of approximately 130 t/h about an hour before midnight, and then decreasing back to near-zero values in the early morning. Scan 00, on the other hand, shows a similar pattern in the evening of the 13th, but reaches a comparatively low value (40 t/h) at the time when the other two scans peak. It then reaches its own peak of 138 t/h, comparable in magnitude to that of scans 03 and 04, slightly after midnight. This suggests that the emission estimate from scan 00 is shifted by approximately one hour relative to the other two.

This apparent temporal shift can also be observed on 15th November, with an even larger shift of approximately 3 h. For the remaining three days with substantial scan overlap, the results are more divergent. On the 8th, the agreement between scans is

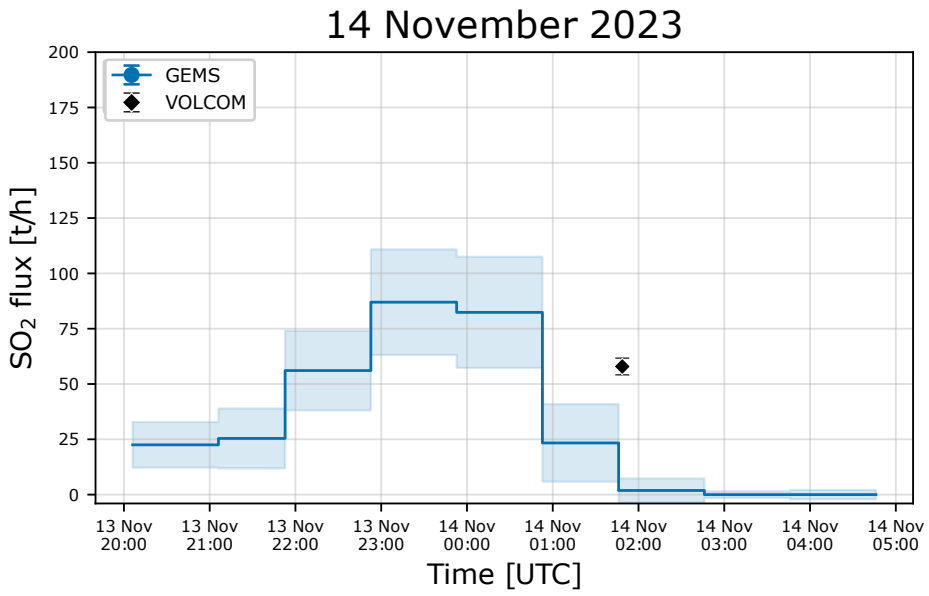



**Figure 4.8:** Resulting $SO_2$ flux from the combination of individual scans acquired on 14 November 2023. The shaded area represents the propagated uncertainty. The black scattered point shows the $SO_2$ flux estimated during the VOLCOM campaign, which is discussed in the following section.

poor: two scans show values markedly different from the other three, with the latter averaging around 23 t/h in the morning of the day, compared to approximately 121 t/h for the former two. Results from 3rd and 4th November are more promising in terms of agreement; although estimates on the morning of the 4th still show some variability, all scans consistently captured an increase in the signal.

Moreover, the estimated fluxes are not always consistent within their respective uncertainties, suggesting that the propagated uncertainty considered in Section 3.3.2.1 may be underestimated.

The resulting flux estimates are likely to be biased towards the early morning and daytime hours (local time), as the GEMS instrument requires daylight to acquire observations. Although older portions of the plume can still be used to estimate emissions during the night, the plume may become too dispersed or dynamically unstable to remain reliably traceable throughout the entire night. Consequently, nighttime emissions may be less well represented in the resulting flux time series.

Overall, the two-week period analysed constitutes a limited sample, and a longer dataset would be needed to draw more robust conclusions. To obtain a single representative value for each hour, flux estimates from individual scans are combined following the procedure described in Section 3.3.2, yielding one hourly $SO_2$ flux estimate per day (Fig. 4.8). As the emission start times differ between scans, their mean is calculated and used to define the representative start time of the hourly emission.

The resulting mean $SO_2$ flux exhibits the characteristic bell-shaped curve already

observed in the individual scans. The emission begins in the evening of 13 November, with a flux of approximately 24 t/h, and increases throughout the night, reaching a maximum of approximately 83 t/h between 23:00 and midnight. The flux then decreases until it reaches zero in the morning of 14 November.

The hourly flux estimate is currently calculated as an arithmetic mean of the individual scan estimates, giving equal weight to each scan. However, the individual estimates may not be equally reliable. Estimates obtained closer to the actual scan time are expected to be more representative, as the wind field used for plume transport is more likely to correspond to the conditions at the time of the observation. In contrast, estimates corresponding to times further from the scan time may be more strongly affected by changes in the wind field, including variations in wind direction and increased turbulence. A weighted mean could therefore be considered, assigning greater weight to estimates obtained closer to the scan time and thereby accounting for the expected differences in their reliability.

This averaging procedure was applied to all available days, including cases where the spatial overlap between scans was limited or where the individual scan estimates showed poor agreement. The resulting hourly flux estimates should therefore be interpreted with these limitations in mind. Nevertheless, the available GEMS observations provide a first opportunity to evaluate the performance of the cross-section method against independent ground-based measurements. The comparison with these measurements is presented in the following section.

## 4.2 Comparison with ground-based measurements

The VOLCOM and JMA datasets were converted to a common unit of t/h (Section 3.2.3 and Section 3.2.2). Of the two available JMA measurement days, only the 15th of November could be used, as all GEMS scans on the 6th of November were excluded by the plume-selection algorithm.

The four days discussed below (Fig.4.9) were selected to represent both the general performance of the method and specific limitations identified during the comparison. The VOLCOM data are reported as individual black points with error bars, and the single JMA value is shown as a horizontal black line, since it is representative of the whole day, with the shaded area representing the minimum and maximum measurements of the day (Section 3.2.3).

Ground-based flux estimates from VOLCOM range from approximately 50 t/h and 120 t/h, with most values falling between 80 t/h and 120 t/h. Compared to these, the cross-section method applied to the GEMS product performs well in terms of order of magnitude. However, GEMS-derived estimates are consistently lower than the ground-based ones, with an average underestimation of approximately 50 t/h. In most cases,

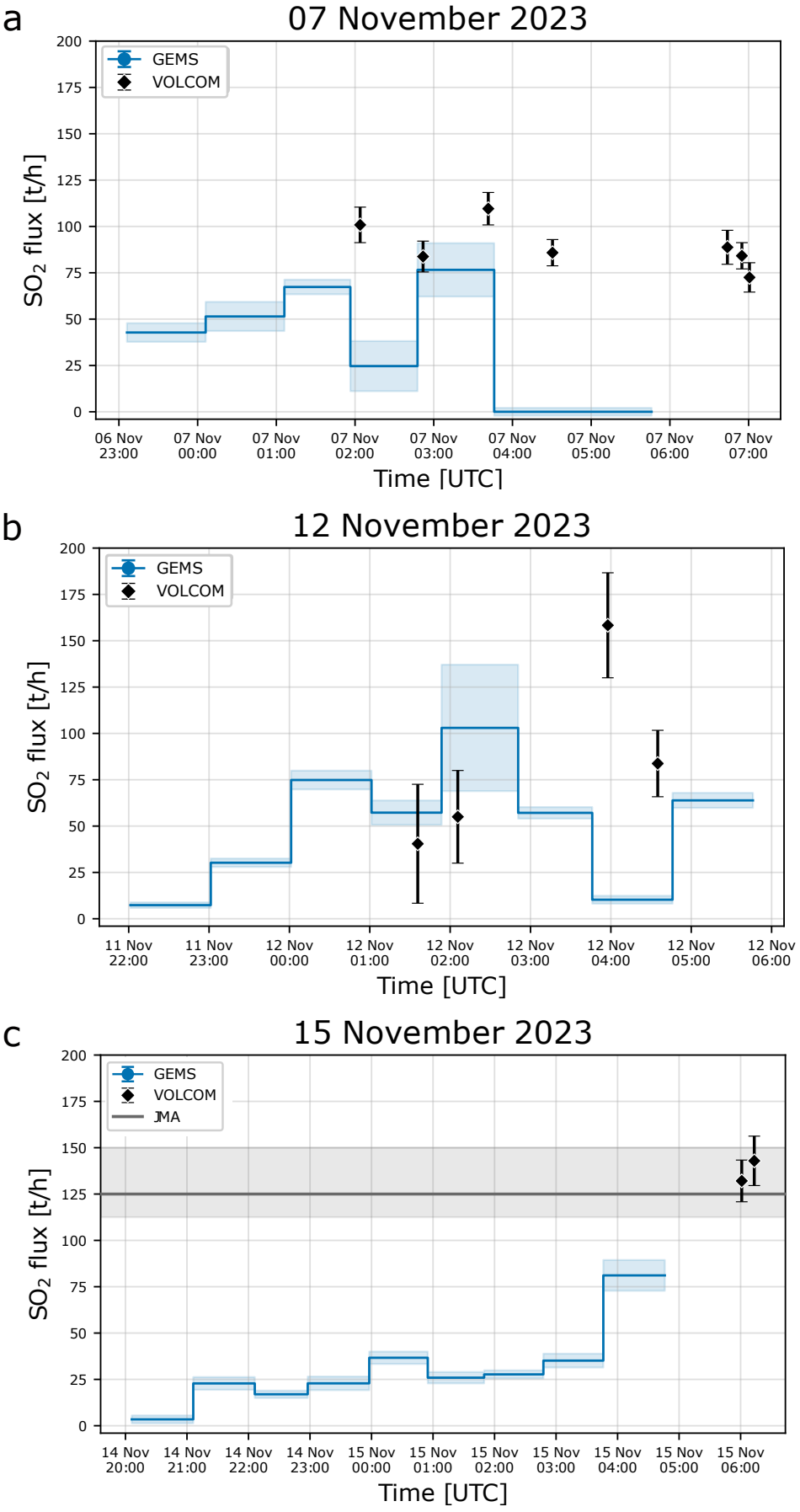



**Figure 4.9:** Examples days for $SO_2$ flux emissions estimates compared to ground-based measurements. a) 07 November 2023. b) 12 November 2023. c) 15 November 2023. The shadow is the propagated uncertainty.

the ground-based measurement lies above the range defined by the GEMS flux estimate and its associated uncertainty. This indicates that the underestimation observed is systematic rather than the result of random error. Several factors may contribute to the lower $SO_2$ fluxes estimated from GEMS compared with the ground-based VOLCOM measurements. One possible source of this discrepancy is the coarser spatial resolution of the GEMS product ($7 \times 16$ km$^2$).If the plume occupies only part of a GEMS pixel, rather than its entire area, the retrieved column density is effectively diluted over the pixel, resulting in a lower apparent VCD and, consequently, a lower estimated flux. In addition, the effective spatial footprint of the GEMS observations may introduce further uncertainty in the estimated flux, as the actual area represented by each observation may differ from the nominal pixel dimensions. If a consistent underestimation is confirmed in future measurement campaigns, these additional observations could provide a basis for deriving an empirical correction factor for GEMS-based flux estimates.

The difference in temporal representativeness between the two measurement approaches may provide another source of discrepancy. The VOLCOM flux estimates are effectively instantaneous, as each transect is completed over a relatively short period and therefore represents the emission at a specific point in time. In contrast, the GEMS-based flux estimates considered here represent hourly averages. Consequently, the two measurements do not necessarily describe the same temporal state of the emission, particularly when the flux varies substantially over the course of an hour.

In addition to these spatial and temporal differences, the quality of the satellite observation may be affected by the conditions along the viewing geometry. Clouds and aerosols between the satellite and the plume can partially obscure the $SO_2$ signal or affect its retrieval, potentially leading to an underestimation of the VCD and hence of the derived flux. The extent to which such effects contribute to the observed discrepancy, however, cannot be quantified from the present analysis. A further consideration concerns the time and location represented by each GEMS flux estimate. While the VOLCOM measurements are made directly across the plume close to the volcano and therefore provide an estimate corresponding closely to the time of the measurement, a GEMS-based estimate assigned to a given hour may be derived from a plume that was emitted substantially earlier and has since been transported downwind. For example, a plume section located 100 km from the volcano at the time of the satellite observation may be used to estimate the emission corresponding to an earlier hour. During this transport period, $SO_2$ may be removed, meaning that the retrieved flux could underestimate the original emission at the source. This potential effect is not explicitly accounted for in the current analysis and could represent an additional source of discrepancy between the GEMS and VOLCOM estimates.

This is particularly relevant given that the assumption of negligible $SO_2$ loss adopted

in this study, based on a fixed atmospheric lifetime of a few days, may not hold uniformly: the $SO_2$ lifetime is known to vary considerably depending on atmospheric conditions such as humidity, oxidant availability, and aerosol load, and could therefore be substantially shorter than assumed under certain conditions, making the resulting bias potentially larger than estimated in Section 3.3.2.

Quantifying this effect would require an analysis of the individual GEMS scans that explicitly accounts for the age of the sampled plume, i.e., the time elapsed between emission at the volcano and observation by the satellite. Such an analysis could help determine whether plume ageing during transport contributes systematically to the lower GEMS-based flux estimates.

## 4.3 Comparison to FLEXPART-WRF model simulation

To further evaluate the GEMS-derived emission estimates, their ability to reproduce the observed spatial distribution of $SO_2$ was assessed using the FLEXPART-WRF dispersion model (hereafter referred to as "the model"). The model was initialized with the hourly mean emission estimates derived from GEMS for 14 November 2023 (Fig. 4.8). The resulting simulated $SO_2$ distribution was then compared with the observations to assess whether the GEMS-derived emission estimates can reproduce the observed plume evolution and spatial extent.

The output of the FLEXPART-WRF model consists of particle trajectories. To compare these with the GEMS product, the trajectories had to be gridded onto the same spatial grid used in the GEMS retrieval.

Each trajectory carries information on its latitude, longitude, height, and mass percentage, together with additional state variables, namely temperature, relative humidity, and density. From these state variables, the pressure at each trajectory position was calculated, in order to make the coordinates comparable with the vertical pressure levels used by the radiative transfer model in the GEMS $SO_2$ retrieval.

The VCD of $SO_2$ from the model was calculated as follows:

1. A GEMS scan was selected, together with its scan time over Sakurajima and the $SO_2$ emission rate estimated for that day from the cross-section method.
2. Since each FLEXPART-WRF simulation is initialised hourly and runs for a duration of 12 h, the 12 simulations preceding the scan were identified, as together they span the period leading up to it.
3. For each of these 12 simulations, the output file closest in time to the scan was selected, representing a snapshot of the simulated plume at that time (output files are written hourly).

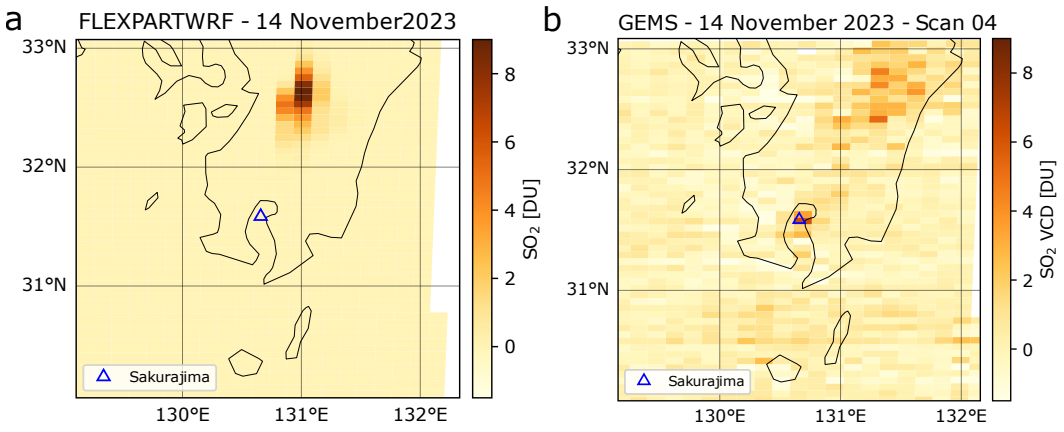



**Figure 4.10:** VCD comparison. a) VCD computed from the FLEXPART-WRF simulation. b) VCD from the GEMS product.

4. The mass percentage of each parcel was multiplied by the $SO_2$ emission rate corresponding to that simulation's own initialisation hour, yielding the total $SO_2$ mass in each parcel.
5. Only parcels tagged with the tracer corresponding to the plume height identified in the scan were retained; each parcel carries a tracer identifying the height at which it was released.
6. Steps 3–5 were repeated for each of the 12 simulations, so that all trajectories contributing to the selected scan were collected.
7. These trajectories were binned onto the GEMS grid, and the $SO_2$ mass was summed over each column to obtain the modelled VCD.

The model VCD is then compared to the GEMS product. As an illustrative example, this comparison is presented for the scan at 04:45 on that day (Fig. 4.10).

The modelled plume is physically plausible: consistent with the fact that the estimated emission at the scan time itself was null, the plume is not located close to the volcano, but rather some distance away. It features a region of high VCD, reaching a maximum of 9 DU, with values decreasing towards the edges of the plume, and extends over 31 pixels on the GEMS grid.

Comparing the two plumes reveals a clear structural difference: the model produces a single, well-defined plume to the north of the volcano, whereas the GEMS retrieval shows two distinct features – a bulk of high-$SO_2$ pixels in a similar location, shifted approximately 50 km further south-west, and an additional plume located close to the volcano itself. This near-source feature is not reproduced by the model, since the corresponding initialisation fluxes were close to zero near the scan time, with emissions present only further back in time (Fig. 4.8). This discrepancy stems from a known

limitation of the current plume-detection algorithm (Section 4.1.1), which retains only a single, spatially coherent group of pixels per scan, and therefore cannot capture near-source emissions occurring separately from the main plume.

For the distant plume, which is present in both datasets, the two show comparable magnitude and differ mainly in two respects. First, the model reaches a slightly higher maximum VCD (9 DU) than the GEMS retrieval (5.5 DU). Second, the two plumes differ in spatial extent, with the GEMS plume covering 58 pixels compared to 31 pixels in the model. Both differences may be explained by the fact that, in reality, $SO_2$ is unlikely to be emitted at a single altitude, as assumed in the model initialisation, but rather across a range of heights. As these portions of the plume are transported under different atmospheric conditions, the resulting plume could spread more than simulated here – consistent with the larger extent and lower peak concentration observed in the GEMS retrieval, since a more spread-out plume corresponds to a lower column density for the same total mass.

Overall, the mean emissions derived from GEMS were able to reproduce a plume of comparable VCD magnitude and general transport direction using the FLEXPART-WRF model, although the modelled plume is more concentrated and does not capture the near-source feature visible in the GEMS retrieval – a discrepancy directly linked to the plume-selection limitation discussed above.

An important detail to note is that, in the model, the VCD is obtained simply by summing the $SO_2$ mass in the vertical direction. For a satellite retrieval, however, this is not the case: the DOAS method yields the SCD, which must then be divided by the AMF to obtain the VCD. The AMF, among other parameters, incorporates an assumed vertical distribution of $SO_2$, since the satellite's sensitivity to the gas varies with altitude. As a result, the accuracy of the GEMS VCD depends on how well the assumed vertical profile matches the true one.

To estimate the GEMS VCD that would have been retrieved had the true $SO_2$ vertical profile matched the one simulated by FLEXPART-WRF, a modified air mass factor ($AMF_{new}$) was computed for each GEMS pixel, following Eskes and Boersma [2003], using the normalised vertical profile derived from the model.

$$\mathrm{AMF}_{\mathrm{new}} = \vec{\mathrm{BAMF}} \cdot \vec{V_p} = \sum_i \mathrm{BAMF}_i \cdot V_{p,i} \tag{4.1}$$

where $\vec{\mathrm{BAMF}}$ is the box AMF profile from GEMS, and $\vec{V_p}$ is the normalised FLEXPART-WRF vertical profile.

The $\vec{\mathrm{BAMF}}$ can be calculated from the averaging kernel (AK) of GEMS and the original AMF, $AMF_o$, as:

$$\vec{\mathrm{BAMF}} = \mathrm{AMF}_{\mathrm{o}} \cdot \vec{\mathrm{AK}} \tag{4.2}$$

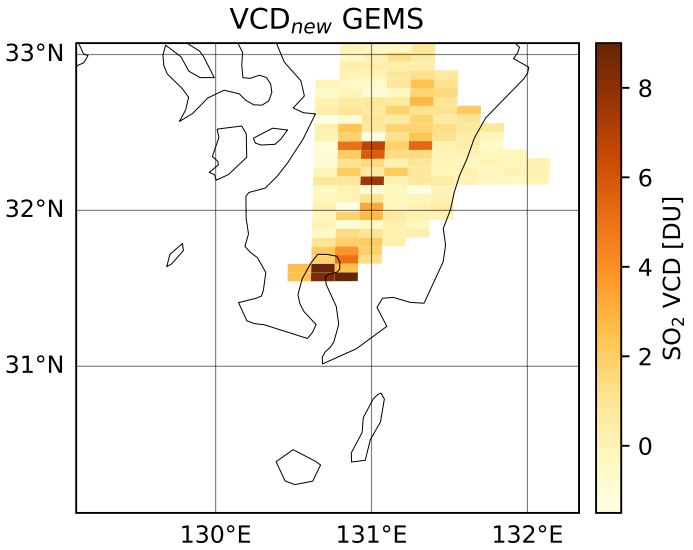



**Figure 4.11:** New GEMS VCD, computed using the vertical profile from the FLEXPART-WRF simulation.

Substituting Eq. 4.2 into Eq. 4.1, $\mathrm{AMF_{new}}$ becomes:

$$\mathrm{AMF_{new}} = \mathrm{AMF_o} \sum_i \mathrm{AK}_i \cdot V_{p,i} \tag{4.3}$$

$\mathrm{AMF_{new}}$ was then used to compute the new VCD from the original SCD ($\mathrm{SCD_o}$) as:

$$\mathrm{VCD_{new}} = \frac{\mathrm{SCD_o}}{\mathrm{AMF_{new}}} \tag{4.4}$$

In regions where the modelled vertical profile is zero throughout the column, the corresponding normalised profile is undefined; these pixels were therefore set to NaN to avoid division by zero. The resulting new GEMS VCD, $\mathrm{VCD_{new}}$, is shown in Fig. 4.11.

In $\mathrm{VCD_{new}}$, the plume that was clearly visible farther downwind from the volcano in the original retrieval is no longer distinguishable from the surrounding background. In contrast, the signal close to the volcano is enhanced. A weak signal extending downwind in the direction of the wind is also visible, providing a faint indication of the plume. However, the plume predicted by the model is not apparent in the new retrieval. This comparison illustrates how strongly the choice of a priori profile information can influence the outcome of the retrieval.

To investigate the cause of these differences, the original and new AMFs were compared (Fig. 4.12). The colour scales were not unified because the two AMFs span different value ranges. The original GEMS AMF is below 1 throughout the scene, with

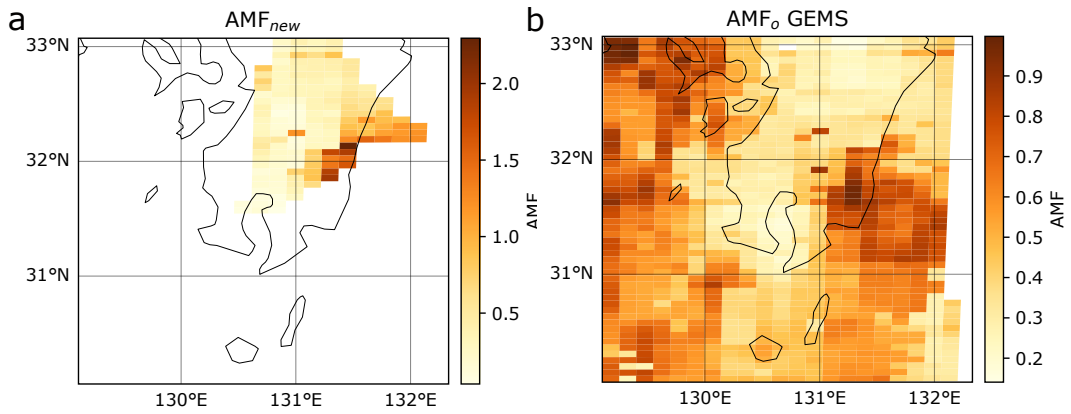



**Figure 4.12:** Comparison AMF. a) $AMF_{new}$, recalculated using the normalised vertical profile from FLEXPART-WRF. b) The original AMF from the GEMS retrieval.

particularly low values of approximately 0.1–0.4 in the region corresponding to the identified plume. In contrast, $AMF_{new}$ reaches values around 1 or higher in this region. This substantial difference in the AMF therefore provides a possible explanation for the changes observed in the retrieved VCD.

To understand the source of this difference, the normalized vertical distributions from FLEXPART-WRF and the box AMFs (BAMF) from the GEMS scan are shown in Fig. 4.13 for three representative pixels: one located over Sakurajima, one at the centre of the plume simulated by the model, and one at the centre of the plume identified in the original GEMS VCD. The total AMF for each pixel is shown in the final panel.

The normalized vertical profile shows that, at the time of the scan, the modelled distribution over Sakurajima was concentrated at low altitude, centred around 1000 hPa. The model plume pixel shows a wider distribution, spanning from 900 to 700 hPa and centred around 800 hPa. The pixel corresponding to the original GEMS plume shows a comparatively narrow distribution, centred at 850 hPa.

The box AMF profiles are quite similar across the three pixels, with low values near the surface and higher values aloft, and a step-like increase at approximately 750 hPa; this feature likely reflects an assumed aerosol layer at that altitude in the GEMS retrieval algorithm. From the resulting total AMF values for each pixel, it can be seen that the higher the assumed altitude of the $SO_2$, the higher the resulting AMF.

The low AMF values in the original GEMS retrieval are therefore likely explained by an assumed $SO_2$ altitude considerably lower than that of the actual volcanic plume. This is consistent with the fact that the current GEMS $SO_2$ retrieval does not explicitly account for the location of volcanic sources: $SO_2$ in the atmosphere is likely assumed to originate primarily from anthropogenic sources, and is therefore expected to be concentrated close to the ground.

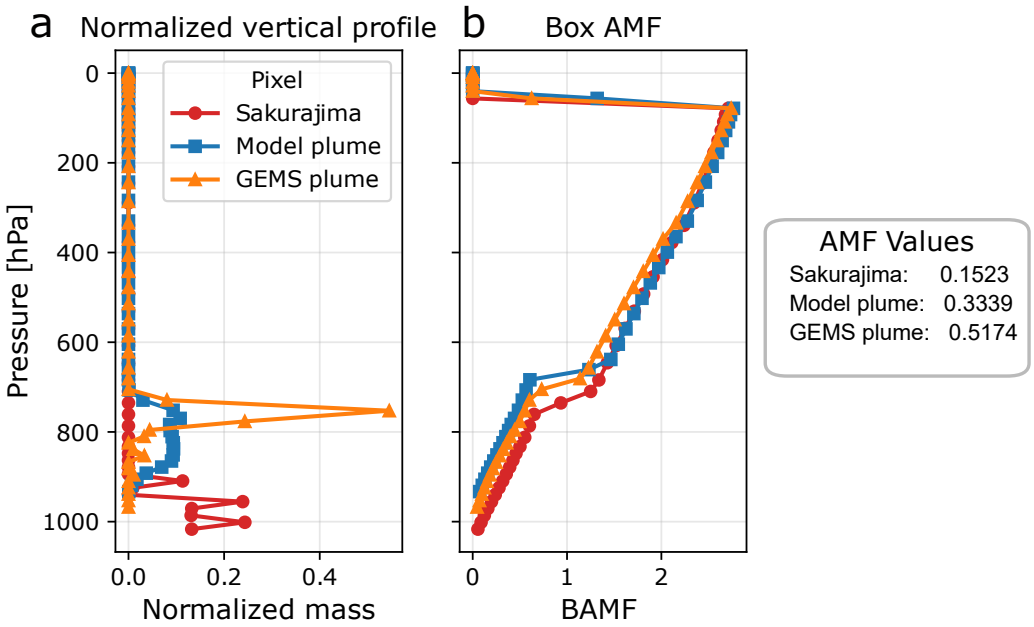



**Figure 4.13:** a) FLEXPART-WRF Normalised vertical distribution. b) Box AMF from the GEMS product. The AMF box reports the AMF for the individual pixels.

Taken together, these results show that the emission record derived from GEMS was able to reproduce a plume with a similar transport direction and comparable magnitude, albeit somewhat lower, to the one observed by GEMS, but with a spatial mismatch of approximately 50 km in plume location. This mismatch implies that $AMF_{new}$, computed using the vertical profile from the FLEXPART-WRF plume, may not be a good estimator for the a priori distribution, since it corresponds to a different location than the actual plume. Nonetheless, recomputing the VCD using this profile showed that the $SO_2$ VCD retrieved by the operational GEMS product for this volcanic plume is highly sensitive to the assumed vertical distribution of the gas. This suggests that, if the true vertical distribution of volcanic $SO_2$ is indeed elevated, as simulated by FLEXPART-WRF, the operational GEMS product may be overestimating the $SO_2$ VCD, since it assumes a lower-altitude vertical profile. This would imply that the true emission flux is potentially even lower than the estimates presented in this study, further increasing the discrepancy with respect to the ground-based measurements observed in Section 4.2, rather than explaining it.

# Chapter 5

# Conclusions & outlook

This thesis addresses the problem of estimating $SO_2$ emission fluxes at high temporal resolution, a topic relevant to the health of populations living near volcanoes, since $SO_2$ and its reaction products are harmful to both human health and the environment.

Sakurajima, in Japan, one of the most active volcanoes in the country, was chosen as the study case due to the high population density in the surrounding area, and because ground-based $SO_2$ flux measurements were available from the VOLCOM campaign, conducted between the 3th and the 16th November 2023–the same period analysed in this study.

This work was structured around three objectives: (1) estimating $SO_2$ emission flux from Sakurajima using GEMS data and the cross-section method; (2) validating the resulting estimates against ground-based measurements from JMA and the VOLCOM campaign; and (3) assessing the feasibility of reproducing the observed $SO_2$ plume using FLEXPART-WRF, driven by the estimated $SO_2$ emission flux.
The main findings of this work can be summarised as follows.

It was possible to delineate a plume and draw transects on the GEMS VCD scans for 49% of the analysed cases. The remaining scans were discarded primarily due to excessive retrieval noise or unstable wind conditions. In addition, for scans where the plume was spatially divided into two or more disconnected groups of pixels, only the group closest to the source was retained for the analysis – a limitation of the current selection algorithm, which does not yet account for intermitting emissions, potentially leading to an underestimation of the resulting flux. In one case, the algorithm also selected a feature that was likely a retrieval artefact rather than a genuine volcanic plume, highlighting the need for additional exclusion criteria in future refinements of the method. For days with sufficient scan coverage, the resulting hourly flux estimates showed a consistent temporal trend, with values ranging from 0 to 140 t/h. One notably higher value of 200 t/h was also observed, attributed to a known limitation of the method when part of the plume lies upwind of the source.

The comparison with ground-based measurements from the VOLCOM campaign re-

vealed a systematic underestimation of the GEMS-derived flux, on the order of 50 t/h, which was not accounted for by the propagated uncertainty. This discrepancy is hypothesised to be related, at least in part, to the coarse spatial resolution of the GEMS $SO_2$ product ($7 \times 16$ km$^2$), which may dilute the retrieved column density when the plume covers only a fraction of a pixel. In addition, VOLCOM measurements represent a single moment in time, whereas each GEMS estimate reflects conditions integrated over the corresponding scan period; short-lived emission peaks may therefore be smoothed out in the flux derived from the GEMS product, further contributing to the observed underestimation. A further point concerns the age of the sampled plume: since GEMS-based flux estimates for a given hour may originate from plume sections emitted, and transported, several hours earlier, any chemical loss occurring during this transport is not captured by the current analysis. This is particularly relevant given that the $SO_2$ lifetime can vary considerably with atmospheric conditions, and may therefore be shorter than assumed under the fixed-lifetime approximation adopted in this study, representing an additional source of underestimation not accounted for in the current analysis.

Finally, the estimated hourly emissions were used to initialise the FLEXPART-WRF transport model, in order to assess whether the plume pattern observed by GEMS could be reproduced. The model was able to reproduce a plume of similar magnitude, slightly higher than the one retrieved by GEMS – possibly reflecting differences in the assumed emission height, and therefore in atmospheric conditions and dispersion – as well as comparable spatial extent and transport direction downwind of the volcano, although with a spatial shift of approximately 50 km.

Moreover, using the vertical distribution obtained from the model to recompute the GEMS VCD showed that the retrieved $SO_2$ VCD is highly sensitive to the assumed a priori vertical profile used to convert the SCD into the VCD, and that the current operational GEMS retrieval likely assumes a vertical distribution more representative of anthropogenic sources than of elevated volcanic plumes. This finding suggests that the AMF used in the operational product may not be well suited to volcanic sources, and could constitute an additional, currently unquantified, source of bias in the retrieved flux.

**Outlook**

Looking ahead, these results indicate that GEMS is a promising tool for high-temporal-resolution monitoring of volcanic $SO_2$ emissions, although its operational product currently underestimates the resulting flux estimates. Addressing this would require further work in several directions: extending the plume-selection algorithm to handle spatially divided plumes and multiple emission heights within a single scan; developing a volcano-specific a priori vertical profile for the AMF calculation, tailored to elevated

degassing sources rather than ground-level anthropogenic emissions; and evaluating the observed bias over a longer analysis period, covering a wider range of degassing conditions.

Finally, the FLEXPART-WRF simulations performed in this study could be extended into a Bayesian inverse modelling framework, in order to identify the emission rate and plume height that best reproduce the observed $SO_2$ signal. This would provide an independent estimate of the emission flux, complementary to the one obtained in this study.

# Appendix A

# Additional materials

# A ADDITIONAL MATERIALS

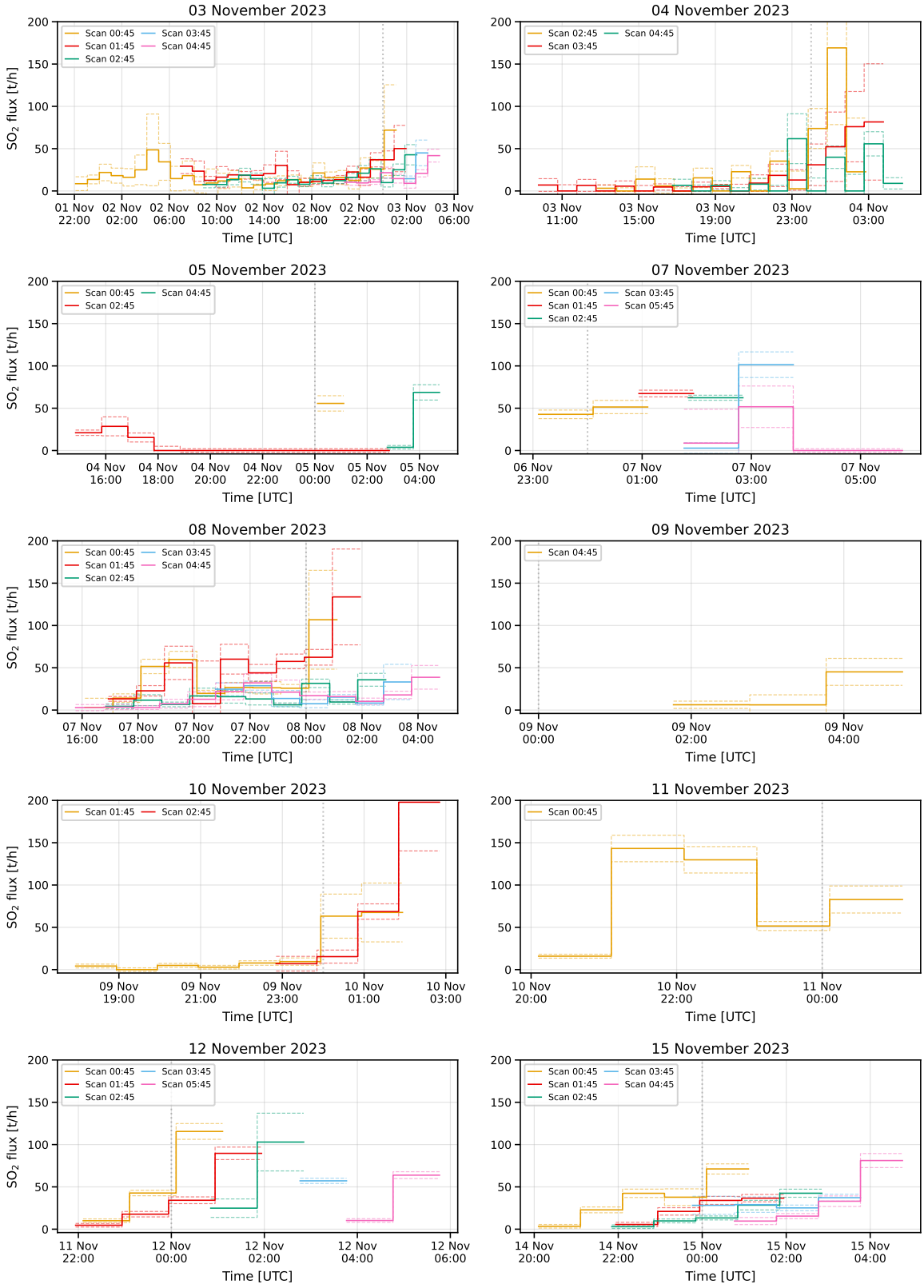



**Figure A.1:** $SO_2$ flux estimates for all scans passing the selection criteria. Dotted lines indicate the uncertainty; the shaded area has been removed from this figure for clarity.

# Bibliography

Brioude, J., Arnold, D., Stohl, A., Cassiani, M., Morton, D., Seibert, P., Angevine, W., Evan, S., Dingwell, A., Fast, J. D., Easter, R. C., Pisso, I., Burkhart, J., and Wotawa, G.: The Lagrangian Particle Dispersion Model FLEXPART-WRF Version 3.1, Geoscientific Model Development, 6, 1889–1904, https://doi.org/10.5194/gmd-6-1889-2013, 2013.

Budd, L., Griggs, S., Howarth, D., and Ison, S.: A Fiasco of Volcanic Proportions? Eyjafjallajökull and the Closure of European Airspace, Mobilities, 6, 31–40, https://doi.org/10.1080/17450101.2011.532650, 2011.

Carlsen, H. K., Hauksdottir, A., Valdimarsdottir, U. A., Gíslason, T., Einarsdottir, G., Runolfsson, H., Briem, H., Finnbjornsdottir, R. G., Gudmundsson, S., Kolbeinsson, T. B., et al.: Health Effects Following the Eyjafjallajökull Volcanic Eruption: A Cohort Study, BMJ open, 2, e001 851, https://doi.org/10.1136/bmjopen-2012-001851, 2012.

Chou, M.-D. and Suarez, M. J.: An Efficient Thermal Infrared Radiation Parameterization for Use in General Circulation Models, 1994.

Dudhia, J.: A Multi-Layer Soil Temperature Model for MM5, Preprints, The Sixth PSU/NCAR Mesoscale Model Users' Workshop, pp. 22–24, 1996.

Eatough, D., Caka, F., and Farber, R.: The Conversion of $SO_2$ to Sulfate in the Atmosphere, Israel Journal of Chemistry, 34, 301–314, https://doi.org/10.1002/ijch.199400034, 1994.

ESC: Environmental Satellite Center, URL https://nesc.nier.go.kr.

Eskes, H. J. and Boersma, K. F.: Averaging Kernels for DOAS Total-Column Satellite Retrievals, Atmospheric Chemistry and Physics, 3, 1285–1291, https://doi.org/10.5194/acp-3-1285-2003, 2003.

European Centre for Medium-Range Weather Forecasts: ERA5: Data Documentation, URL https://confluence.ecmwf.int/spaces/CKB/pages/76414402/ERA5+data+documentation#ERA5:datadocumentation-Introduction.

Galle, B., Johansson, M., Rivera, C., Zhang, Y., Kihlman, M., Kern, C., Lehmann, T., Platt, U., Arellano, S., and Hidalgo, S.: Network for Observation of Volcanic and Atmospheric Change (NOVAC)—A Global Network for Volcanic Gas Monitoring: Network Layout and Instrument Description, Journal of Geophysical Research: Atmospheres, 115, https://doi.org/10.1029/2009JD011823, 2010.

Gudmundsson, M. T., Thordarson, T., Höskuldsson, Á., Larsen, G., Björnsson, H., Prata, F. J., Oddsson, B., Magnússon, E., Högnadóttir, T., Petersen, G. N., et al.: Ash Generation and Distribution from the April-May 2010 Eruption of Eyjafjallajökull, Iceland, Scientific reports, 2, 572, https://doi.org/10.1038/srep00572, 2012.

Hersbach, H., Bell, B., Berrisford, P., Hirahara, S., Horányi, A., Muñoz-Sabater, J., Nicolas, J., Peubey, C., Radu, R., Schepers, D., Simmons, A., Soci, C., Abdalla, S., Abellan, X., Balsamo, G., Bechtold, P., Biavati, G., Bidlot, J., Bonavita, M., De Chiara, G., Dahlgren, P., Dee, D., Diamantakis, M., Dragani, R., Flemming, J., Forbes, R., Fuentes, M., Geer, A., Haimberger, L., Healy, S., Hogan, R. J., Hólm, E., Janisková, M., Keeley, S., Laloyaux, P., Lopez, P., Lupu, C., Radnoti, G., De Rosnay, P., Rozum, I., Vamborg, F., Villaume, S., and Thépaut, J.-N.: The ERA5 Global Reanalysis, Quarterly Journal of the Royal Meteorological Society, 146, 1999–2049, https://doi.org/10.1002/qj.3803, 2020.

Hong, S.-Y., Dudhia, J., and Chen, S.-H.: A Revised Approach to Ice Microphysical Processes for the Bulk Parameterization of Clouds and Precipitation, Monthly Weather Review, 132, 103–120, https://doi.org/10.1175/1520-0493(2004)132⟨0103:ARATIM⟩2.0.CO;2, 2004.

Iguchi, M., Yamada, T., and Tameguri, T.: Sequence of Volcanic Activity of Sakurajima Volcano, Japan, as Revealed by Non-Eruptive Deflation, Frontiers in Earth Science, 10, 727 909, https://doi.org/10.3389/feart.2022.727909, 2022.

Japan Meteorological Agency: Volcanic Activity Explanatory Material (December 2023) – Sakurajima, URL https://www.data.jma.go.jp/vois/data/report/monthly_v-act_doc/fukuoka/23m12/506_23m12.pdf, 2024.

Jiménez, P. A., Dudhia, J., González-Rouco, J. F., Navarro, J., Montávez, J. P., and García-Bustamante, E.: A Revised Scheme for the WRF Surface Layer Formulation, Monthly Weather Review, 140, 898–918, https://doi.org/10.1175/MWR-D-11-00056.1, 2012.

Kain, J. S.: The Kain–Fritsch Convective Parameterization: An Update, Journal of Applied Meteorology, 43, 170–181, https://doi.org/10.1175/1520-0450(2004)043⟨0170:TKCPAU⟩2.0.CO;2, 2004.

Kern, C.: Ultraviolet and Visible Remote Sensing of Volcanic Gas Emissions, Journal of Volcanology and Geothermal Research, 468, 108 423, https://doi.org/10.1016/j.jvolgeores.2025.108423, 2025.

Kim, J., Jeong, U., Ahn, M.-H., Kim, J. H., Park, R. J., Lee, H., Song, C. H., Choi, Y.-S., Lee, K.-H., Yoo, J.-M., et al.: New Era of Air Quality Monitoring from Space: Geostationary Environment Monitoring Spectrometer (GEMS), Bulletin of the American Meteorological Society, 101, E1–E22, https://doi.org/10.1175/BAMS-D-18-0013.1, 2020.

Lee, C., Martin, R. V., Van Donkelaar, A., Lee, H., Dickerson, R. R., Hains, J. C., Krotkov, N., Richter, A., Vinnikov, K., and Schwab, J. J.: $SO_2$ Emissions and Lifetimes: Estimates from Inverse Modeling Using in Situ and Global, Space-Based (SCIAMACHY and OMI) Observations, Journal of Geophysical Research, 116, D06 304, https://doi.org/10.1029/2010JD014758, 2011.

Lin, J. C., Gerbig, C., Wofsy, S. C., Andrews, A. E., Daube, B. C., Davis, K. J., and Grainger, C. A.: A Near-field Tool for Simulating the Upstream Influence of Atmospheric Observations: The Stochastic Time-Inverted Lagrangian Transport (STILT) Model, Journal of Geophysical Research: Atmospheres, 108, 2002JD003 161, https://doi.org/10.1029/2002JD003161, 2003.

Marshak, A., Herman, J., Adam, S., Karin, B., Carn, S., Cede, A., Geogdzhayev, I., Huang, D., Huang, L.-K., Knyazikhin, Y., et al.: Earth Observations from DSCOVR EPIC Instrument, Bulletin of the American Meteorological Society, 99, 1829–1850, https://doi.org/10.1175/BAMS-D-17-0223.1, 2018.

Matsui, T., Zhang, S. Q., Lang, S. E., Tao, W.-K., Ichoku, C., and Peters-Lidard, C. D.: Impact of Radiation Frequency, Precipitation Radiative Forcing, and Radiation Column Aggregation on Convection-Permitting West African Monsoon Simulations, Climate Dynamics, 55, 193–213, https://doi.org/10.1007/s00382-018-4187-2, 2020.

Merucci, L., Burton, M., Corradini, S., and Salerno, G. G.: Reconstruction of SO2 Flux Emission Chronology from Space-Based Measurements, Journal of Volcanology and Geothermal Research, 206, 80–87, https://doi.org/10.1016/j.jvolgeores.2011.07.002, 2011.

Miguez-Macho, G., Stenchikov, G. L., and Robock, A.: Spectral Nudging to Eliminate the Effects of Domain Position and Geometry in Regional Climate Model Simulations, Journal of Geophysical Research: Atmospheres, 109, 2003JD004 495, https://doi.org/10.1029/2003JD004495, 2004.

Mlawer, E. J., Taubman, S. J., Brown, P. D., Iacono, M. J., and Clough, S. A.: Radiative Transfer for Inhomogeneous Atmospheres: RRTM, a Validated Correlated-k Model for the Longwave, Journal of Geophysical Research: Atmospheres, 102, 16 663–16 682, https://doi.org/10.1029/97JD00237, 1997.

Oppenheimer, C., Scaillet, B., and Martin, R. S.: Sulfur Degassing from Volcanoes: Source Conditions, Surveillance, Plume Chemistry and Earth System Impacts, Reviews in mineralogy and geochemistry, 73, 363–421, https://doi.org/10.2138/rmg.2011.73.13, 2011.

Platt, U. and Stutz, J.: Differential Absorption Spectroscopy, in: Differential Optical Absorption Spectroscopy, pp. 135–174, Springer Berlin Heidelberg, Berlin, Heidelberg, https://doi.org/10.1007/978-3-540-75776-4_6, 2008.

Poulidis, A. P. and Iguchi, M.: Model Sensitivities in the Case of High-Resolution Eulerian Simulations of Local Tephra Transport and Deposition, Atmospheric Research, 247, 105 136, https://doi.org/10.1016/j.atmosres.2020.105136, 2021.

Poulidis, A. P., Takemi, T., Iguchi, M., and Renfrew, I. A.: Orographic Effects on the Transport and Deposition of Volcanic Ash: A Case Study of Mount Sakurajima, Japan, Journal of Geophysical Research: Atmospheres, 122, 9332–9350, https://doi.org/10.1002/2017JD026595, 2017.

Poulidis, A. P., Bittner, S., Richter, A., and Vrekoussis, M.: On the Monitoring and Modeling of Volcanic Emissions, IUP Bremen, URL https://www.iup.uni-bremen.de/eng/institute/image-of-the-month/2022---2023/, 2023.

Robock, A.: Volcanic Eruptions and Climate, Reviews of geophysics, 38, 191–219, https://doi.org/10.1029/1998RG000054, 2000.

Seinfeld, J. H. and Pandis, S. N.: Atmospheric Chemistry and Physics: From Air Pollution to Climate Change, John Wiley & Son, Hoboken, New Jersey, 3rd edn., 2016.

Seo, S., Valks, P., Lutz, R., Heue, K.-P., Hedelt, P., Molina García, V., Loyola, D., Lee, H., and Kim, J.: Tropospheric $NO_2$ Retrieval Algorithm for Geostationary Satellite Instruments: Applications to GEMS, Atmospheric Measurement Techniques, 17, 6163–6191, https://doi.org/10.5194/amt-17-6163-2024, 2024.

Shin, H. H. and Hong, S.-Y.: Representation of the Subgrid-Scale Turbulent Transport in Convective Boundary Layers at Gray-Zone Resolutions, Monthly Weather Review, 143, 250–271, https://doi.org/10.1175/MWR-D-14-00116.1, 2015.

Sigl, M., Winstrup, M., McConnell, J. R., Welten, K. C., Plunkett, G., Ludlow, F., Büntgen, U., Caffee, M., Chellman, N., Dahl-Jensen, D., et al.: Timing and Climate Forcing of Volcanic Eruptions for the Past 2,500 Years, Nature, 523, 543–549, https://doi.org/10.1038/nature14565, 2015.

Skamarock, W. C., Klemp, J. B., Dudhia, J., Gill, D. O., Liu, Z., Berner, J., Wang, W., Powers, J. G., Duda, M. G., Barker, D. M., and Huang, X.-Y.: A Description of the Advanced Research WRF Model Version 4, https://doi.org/10.5065/1DFH-6P97, 2019.

Small, C. and Naumann, T.: The Global Distribution of Human Population and Recent Volcanism, Global Environmental Change Part B: Environmental Hazards, 3, 93–109, https://doi.org/10.1016/S1464-2867(02)00002-5, 2001.

Statistics Bureau: 2025 Population Census of Japan — Preliminary Counts of the Population and Households, Ministry of Internal Affairs and Communications, URL https://www.e-stat.go.jp/en/dbview?sid=0004050397, 2025.

Stewart, C., Damby, D. E., Horwell, C. J., Elias, T., Ilyinskaya, E., Tomašek, I., Longo, B. M., Schmidt, A., Carlsen, H. K., Mason, E., et al.: Volcanic Air Pollution and Human Health: Recent Advances and Future Directions, Bulletin of Volcanology, 84, 11, https://doi.org/10.1007/s00445-021-01513-9, 2022.

Stoiber, R. E. and Jepsen, A.: Sulfur Dioxide Contributions to the Atmosphere by Volcanoes, Science, 182, 577–578, https://doi.org/10.1126/science.182.4112.577, 1973.

Theys, N., Campion, R., Clarisse, L., Brenot, H., van Gent, J., Dils, B., Corradini, S., Merucci, L., Coheur, P.-F., Van Roozendael, M., Hurtmans, D., Clerbaux, C., Tait, S., and Ferrucci, F.: Volcanic $SO_2$ Fluxes Derived from Satellite Data: A Survey Using OMI, GOME-2, IASI and MODIS, Atmospheric Chemistry and Physics, 13, 5945–5968, https://doi.org/10.5194/acp-13-5945-2013, 2013.

Theys, N., Hedelt, P., De Smedt, I., Lerot, C., Yu, H., Vlietinck, J., Pedergnana, M., Arellano, S., Galle, B., Fernandez, D., et al.: Global Monitoring of Volcanic SO2 Degassing with Unprecedented Resolution from TROPOMI Onboard Sentinel-5 Precursor, Scientific reports, 9, 2643, https://doi.org/10.1038/s41598-019-39279-y, 2019.

Wei, H.: Health, Wellness, and Quality of Life in Volcanic Communities: A Comprehensive Review of Risks and Protective Strategies, Well-Being Sciences Review, 1, 97–106, https://doi.org/10.54844/wsr.2025.1003, 2025.

BIBLIOGRAPHY

# Acknowledgments

This study was conducted using GEMS (Geostationary Environment Monitoring Spectrometer) data provided by the Environmental Satellite Center of the National Institute of Environmental Research (NIER), under grant NIER-2025-01-03-003 (Operation of the Geostationary Environmental Satellite Ground Station and Satellite Data Service).

I would like to thank A. P. Poulidis, S. Bittner, A. Richter, and M. Vrekoussis for providing the VOLCOM campaign data.

I would also like to thank the Japan Meteorological Agency (JMA) for providing ground-based measurements.

This study was conducted using data from ERA5, produced by the European Centre for Medium-Range Weather Forecasts (ECMWF).

The simulations and data analysis presented in this study were performed on the HPC cluster Aether at the University of Bremen, financed by the German Research Foundation (DFG) within the scope of the Excellence Initiative.

I would like to thank my supervisors for their guidance and for everything they have taught me during this work.

I would also like to thank Alex for his support with the modelling part of this work, and Thomas for proof reading this work. And Rasmus for the template of latex, without it , it would have been a lot uglyer.

Thank you also to everyone in the LAMOS and DOAS groups for always being ready to help – your door has always been open, and it made a real difference.